-

SYNTHESIS, STRUCTURE, AND PROPERTIES OF METASTABLE HETEROSTRUCTURES CONTAINING $TiSe_2$

by

ALEXANDER C. LYGO

A THESIS

Presented to the Department of Chemistry and Biochemistry
and the Robert D. Clark Honors College
in partial fulfillment of the requirements for the degree of
Bachelor of Science

June, 2018

An Abstract of the Thesis of

Alexander C. Lygo for the degree of Bachelor of Science
in the Department of Chemistry and Biochemistry to be taken June, 2018

Title: Synthesis, Structure, and Properties of Metastable Heterostructures Containing $TiSe_2$

Approved: _____

Dr. David C. Johnson

Preparing homologous series of compounds allows chemists to rapidly discover new compounds with predictable structure and properties. Synthesizing compounds within such a series involves navigating a free energy landscape defined by the interactions within and between constituent atoms. Historically, synthesis approaches are typically limited to forming only the most thermodynamically stable compound under the reaction conditions. Presented here is the synthesis, via self-assembly of designed precursors, of isocompositional incommensurate layered compounds $[(BiSe)_{1+\delta}]_m[TiSe_2]_m$ with m =1, 2, and 3. The structure of the BiSe bilayer in the m = 1 compound is not that of the binary compound, and the m = 2 and 3 are the first example of compounds where a BiSe layer thicker than a bilayer in heterostructures have been prepared. Specular and in-plane X-ray diffraction combined with high-resolution electron microscopy data was used to follow the formation of the compounds during low-temperature annealing and the subsequent decomposition of the m = 2 and 3 compounds into $[(BiSe)_{1+\delta}]_1[TiSe_2]_1$ at elevated temperatures. These results show that the structure of the precursor can be used to control reaction kinetics, enabling the synthesis of kinetically stable compounds that are not accessible via traditional techniques. The data collected as a function of temperature and time enabled us to schematically construct the topology of the free energy landscape about the local free energy minima for each of the products.

When the m = 3 compound decomposed, new reflections in the specular diffraction pattern suggested that a heterostructure with a smaller unit cell began to form before it too decomposed to the m = 1 compound. In-plane diffraction indicated that, in addition to BiSe and $TiSe_2$, the compound contained Bi_2Se_3 at all annealing temperatures. To explore if a heterostructure containing BiSe, Bi_2Se_3, and $TiSe_2$ could be synthesized, a series of precursors with the layer sequence $(Bi\text{-}Se)_3$-Ti-Se and varying Bi to Se ratios and layer thicknesses were prepared. Specular diffraction revealed that after annealing numerous precursors formed a compound with a *c*-axis lattice parameter that was consistent with heterostructure containing two BiSe bilayers, one Bi_2Se_3 quintuple-layer, and one $TiSe_2$ trilayer. The electrical properties of this new compound were not that of a simple composite indicating that significant interlayer interactions are present. These results demonstrate that new three component heterostructures can be prepared with controlled nanoarchitecture through self-assembly of designed precursors. The ability to prepare three component heterostructures greatly expands the number of potential new compounds that can be made.

Acknowledgements

I would like to thank my advisor Professor David Johnson for giving me the opportunity to work in his lab and for his mentorship. His guidance and support made this thesis possible. I would like to thank Professor Catherine Page who taught me general chemistry and solid-state chemistry. Without great teachers like her, I would not understand this thesis let alone have written it. I would also like to thank Professor Trond Jacobsen for helping me ensure that this thesis met the requirements of the Clark Honors College.

I would like to thank all the individuals who contributed to this work. I could not have done it alone. I would especially like to thank Suzannah Wood and Danielle Hamann for working with me throughout my undergraduate career. I would like to thank the rest of the Johnson lab for helping me learn and being good friends.

Finally, I would like to thank my parents, my sister, and my girlfriend Christina for their support throughout my undergraduate career.

Table of Contents

List of Figures

List of Tables

Chapter 1: Introduction

The discovery of new compounds with novel physical properties drives many technological advances.[1] Fundamental to predicting new compounds is an understanding of the kinetics and mechanisms of chemical reactions. A great success of molecular organic chemistry is the ability to determine reaction mechanisms and apply that knowledge to design a synthesis route that avoids reaction intermediates that would prevent the formation of the desired molecule. Furthermore, molecular chemists have developed models that inform the design of new molecules with targeted properties. One reason for this success is that typical organic reactions occur at relatively low temperatures (< 100 °C) so it is possible produce kinetically-formed metastable compounds by avoiding the compounds that are global free energy minima.[2]

In contrast, traditional solid-state reactions require long reaction times (24 hrs. to multiple weeks) and reaction temperatures around 1000 ^{O}C to overcome the large activation energy associated with solid-state diffusion. If one considers a simple free energy landscape as shown in Figure 1.1, the large amount of energy used in traditional solid-state reactions will drive a reaction past any metastable products and yield only the thermodynamic or most-stable products. As a result, an enormous number of solid-state compounds are inaccessible via traditional solid-state reactions.[2] A challenge in solid-state chemistry to reduce temperatures and use kinetics to control reactions that yield metastable products.

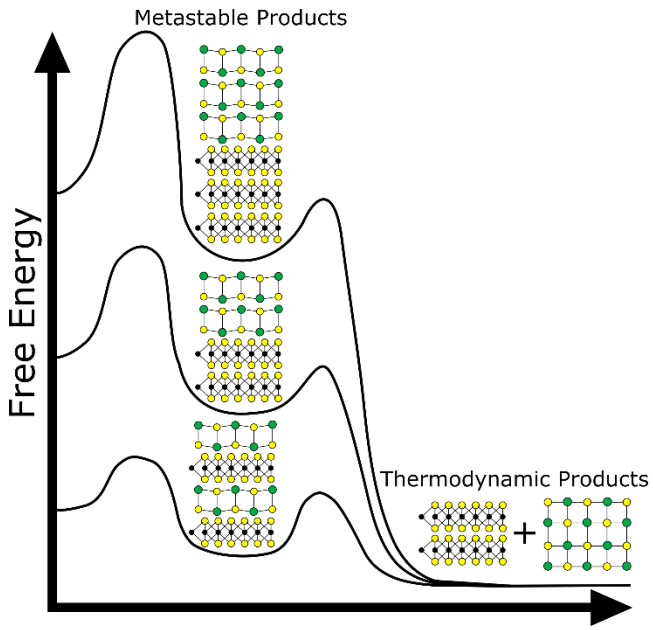

Figure 1.1: Schematic free energy landscape. Metastable compounds are local free energy minima and thermodynamic products are global free energy minima.

Several low temperature synthesis approaches have successfully prepared compounds not accessible via high temperature reactions. The most common approach is to increase diffusion rates by bringing the reaction into the liquid state, typically through the use of fluxes.[3,4] Another approach is to reduce diffusion lengths by preparing a precursor that mix the reactants on atomic length scales, typically via vapor-phase deposition.[5,6] Both of these and other approaches would benefit from more information on the reaction mechanisms and the energy landscape around targeted compounds.

One way of exploring the reaction mechanisms and the free energy landscape is to design series of compounds with systematic structural changes such as heterostructures. Compounds containing van der Waals gaps are well suited for these studies because their lack of dangling bonds and weak interactions across the van der Waals gap yield abrupt interfaces and few defects even with large lattice mismatch.[7]

Additionally, it has been hypothesized that heterostructures formed from quasi 2D materials, such as a monolayers of a van der Waals compound, are local free energy minima.[8] Thus, one can gain knowledge of the free energy landscape and potentially discover many new solid-state materials with predictable structure and properties by systematically changing the thickness of one or more constituents of a van der Waals heterostructure.

One family of van der Waals compounds that are of particular interest to materials scientists are transition metal dichalcogenides (TMDs). These compounds are comprised of covalently bound X-T-X tri-layers where X is a chalcogen and T is a transition metal. TMDs are either metallic, semi-metallic or semiconducting depending on the species of the transition metal and chalcogen.[9] In addition, some TMDs display exotic properties such as superconductivity, charge density waves, and have been observed to be topological semimetals.[10–13] Due to their layered nature, TMDs can be easily incorporated into heterostructures and their thickness can be uniformly scaled by adding or removing any number of tri-layers allowing for sub-nanometer control of a heterostructure's nanoarchitecture. This feature along with their desirable electronic properties make TMDs ideal candidates to replace silicon as the next material for high performance electronic devices. For example, researchers have prepared a 1 nm transistors from a two tri-layers of MoS_2, which is five times smaller than the smallest silicon transistor.[14] Before TMDs and other van der Waals compounds can see wide spread use in devices it is necessary to understand the free energy landscape of heterostructures containing them.

The Johnson Lab synthesizes van der Waals heterostructures using the modulated elemental reactants method. This synthetic approach uses sequential vapor-phase deposition of elements in a high-vacuum chamber to design precursors with compositional modulation mimicking the targeted compound. Upon heating, a precursor with the correct local composition and elemental layer thickness self-assembles into the desired compound as depicted in Figure 1.2. This synthesis route has lead the discovery of a class of metastable compounds referred to as ferecrystals. Most ferecrystals have the general formula $[(MX)_{1+\delta}]_m(TX_2)_n$ where M = Bi, Sn, Pb and X = Se, Te and T is a transition metal.[15] The $1+\delta$ is known as the 'misfit' parameter and is a measure of the difference in the in-plane packing density between the constituents. These compounds are referred to as ferecrystals due to their turbostratic (rotational) disorder between the constituent layers and lack of commensurate interfaces which results in very low lattice thermal conductivity.[16,17] Previously synthesized ferecrystals have been prepared as series of compounds where *m* and *n* are varied nearly limitlessly.[18,19] This ability to vary *m* and *n* enables series of ferecrystals to be prepared with systematic structural modifications, making them an ideal system to use to explore the free energy landscape of metastable compounds.

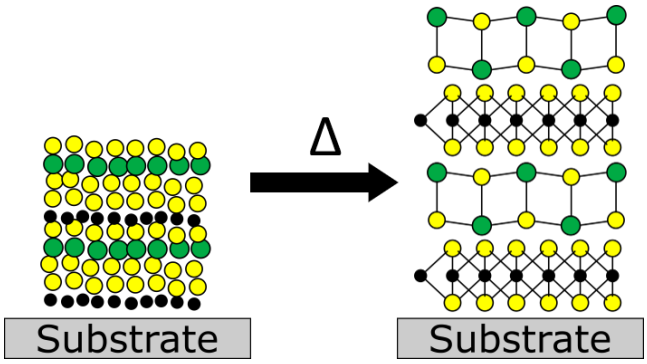

Figure 1.2: Schematic depicting an as-deposited precursor (left) containing M = Bi, Sn, Pb (Green), transition metal (Black), and X = Se, Te (Yellow) forming the targeted heterostructure after gentle heating.

This thesis presents the study of kinetically formed heterostructures containing the transition metal dichalcogenide $TiSe_2$. The first section examines the formation and decomposition of metastable $[(BiSe)_{1+\delta}]_m[TiSe_2]_m$ compounds for m = 1-3. The second investigates the structure and properties of a new heterostructure $(BiSe)_{1+\delta}(Bi_2Se_3)_{1+\gamma}(BiSe)_{1+\delta}TiSe_2$.

Chapter 2: Kinetically-Controlled Formation and Decomposition of Metastable $[(BiSe)_{1+\delta}]_m[TiSe_2]_m$ Compounds.

The work in the following chapter was published 2018-02-12 in *Journal of the American Chemical Society* (DOI: 10.1021/jacs.7b13398). It is coauthored by Danielle Hamann, Daniel Moore, Devin Merrill, Jeffrey Ditto, Marco Esters, Jacob Orlowicz, Suzannah Wood, and David Johnson. Danielle Hamann assisted with preparation of the manuscript. Daniel Moore, Devin Merrill, and Suzannah Wood assisted with sample preparation and collection of in-plane X-ray diffraction data. Jeffrey Ditto assisted with sample preparation for and collection of scanning tunneling electron microscopy data. Marco Esters and Jacob Orlowicz assisted with collection of differential scanning calorimetry data. David Johnson is my advisor and I am the primary author.

Introduction

Homologous series of compounds, compounds related by a common structural module that expands in regular increments, are common in both organic and inorganic chemistry. These series enable chemists to extrapolate chemical information to predict potential structures of compounds that have yet to be prepared. This is particularly important in inorganic chemistry, where examples of homologous series include both simple oxides (M_nO_{2n-1}, where M = Ti, V; Mo_nO_{3n-1}, W_nO_{3n-2}), complex oxides (the Ruddlesden–Popper homologous series, including $Sr_{n+1}M_nO_{3n+1}$, where M = Co, Ti, Ru and Mn), and chalcogenide systems.[4,20–23] The common structural modules that define inorganic homologous series are typically fragments of known structures, such as the rock salt structure. Different structural modules can be obtained from the same bulk

structure simply by altering the direction of fragmentation (such as along 100 or 111 in a rock salt structure).[24] The different building blocks typically lower the total free energy by distorting to create commensurate interfaces. Using chemically stable structural fragments as building blocks to predict structures of novel compounds can be a powerful tool, as illustrated by the work of Cario and coworkers.[25] They used the criteria of commensurate interfaces between two-dimensional building blocks and charge balance to target and discovered new inorganic compounds. However, this approach is not limited to compounds with commensurate interfaces, as compounds with incommensurate interfaces can form if the interaction between layers is large enough to create a local free energy minimum. Perhaps the most studied of these are the misfit layer compounds, which consist of dichalcogenide layers alternating with rock salt structured layers. Inter- and intra- layer interactions cause these compounds to form one commensurate and one incommensurate axis.

The interactions both within and between building blocks define the energy landscape, which contains both global and local free energy minima corresponding to thermodynamically and kinetically stable compounds, respectively.[26,27] At commensurate interfaces, the interactions between layers are defined by the systematic coordination of interfacial atoms by both structural fragments. For a commensurate interface to form, the distorted compound must be lower in free energy than the undistorted analog. At incommensurate interfaces, understanding the interaction between layers is more challenging and has been discussed extensively in the misfit layer compound literature. The consensus is that charge transfer between the layers results in an ionic "capacitive" interaction between the constituents that stabilizes the

structure, although entropic stabilization from cation disorder has also been proposed.[28–33] For an incommensurate interface to form, the interaction between the layers must be large enough to stabilize the compound in spite of the irregular bond distances and angles between atoms at the interface. Utilizing building blocks that readily form incommensurate interfaces significantly expands the number of homologous series that can be imagined.

While homologous series provide the ability to predict potential compounds and their structure, it is often not possible to prepare them via traditional high temperature synthesis methods, which is especially frustrating if one or more members of a potentially homologous series of compounds are known. This is particularly true when the homologous series of compounds have the same overall stoichiometry. A synthetic challenge is to understand how to assemble building blocks and order them into the targeted arrangement. Several low temperature synthesis approaches have successfully been used to prepare compounds not accessible via high temperature solid-state or vapor transport reactions. The most common approach has been using fluxes to reduce reaction temperatures while simultaneously empirically adjusting the composition of the melt, the annealing temperature and annealing time to prepare targeted homologs.[4] Another approach is to first 'prefabricate' structural modules and then find conditions that result in their self-assembly in a desired spatial arrangment.[34] A third method for targeting homologous series is to prepare a designed precursor with compositional periodicity mimicking the desired building blocks and then determine the conditions that allow the compound to self-assemble into the desired product.[35] Additionally, traditional and van der Waals epitaxy have been used to successfully prepare series of

compounds.[7] All of these approaches would benefit from a greater understanding of the reaction mechanisms and the energy landscape around targeted compounds.

Here we study the reaction pathway of precursors designed to form $[(BiSe)_{1+\delta}]_m[TiSe_2]_m$ compounds where m = 1, 2, and 3. $[(BiSe)_{1+\delta}]_1[TiSe_2]_1$ is thermodynamically stable relative to a mix of binary compounds and has been prepared using traditional high temperature solid-state and vapor transport reactions. $[(BiSe)_{1+\delta}]_1[TiSe_2]_1$ prepared at high temperature is a misfit layer compound with one incommensurate axis. It's stability is a consequence of charge transfer from the BiSe layer (containing nominally Bi^{3+} cations) to the $TiSe_2$ layer.[36–38] $[(BiSe)_{1+\delta}]_1[TiSe_2]_1$ has also been prepared from designed precursors, resulting in a rotationally disordered layer compound with two incommensurate axes.[39] $[(BiSe)_{1+\delta}]_m[TiSe_2]_m$ where m = 2, and 3 have not been previously reported and to our knowledge there have been no reports of misfit layer compounds with $m \geq 1$ when the rock salt constituent contains Bi or a trivalent cation such as a lanthanide. Specular X-ray diffraction and in-plane X-ray diffraction data, collected as a function of annealing temperature, revealed the evolution of the super-structure and the structure of the constituents, respectively. High resolution electron microscopy images, collected pre- and post- decomposition, resolved the local structure of the m = 2 compound. All three compounds begin to self-assemble at low temperatures, with $[(BiSe)_{1+\delta}]_2[TiSe_2]_2$ and $[(BiSe)_{1+\delta}]_3[TiSe_2]_3$ decomposing into $[(BiSe)_{1+\delta}]_1[TiSe_2]_1$. $[(BiSe)_{1+\delta}]_m[TiSe_2]_m$ becomes increasing unstable with respect to transforming into $[(BiSe)_{1+\delta}]_1[TiSe_2]_1$ as m is increased. This data was used to construct a schematic free energy landscape containing each of the targeted compounds.

Experimental

Amorphous precursors were synthesized simultaneously on silicon substrates and poly(methyl methacrylate) (PMMA) coated Si wafers, using a custom-built physical vapor deposition system. Elemental Bi and Ti were deposited using electron beam guns and Se was deposited using a Knudsen effusion cell. Pressure was maintained below 5 x 10^{-7} Torr during deposition. The deposition rates of each source and the thickness of the elemental layers were independently measured using quartz crystal microbalances. Computer controlled pneumatic shutters placed above each source regulated the elemental layer thickness and sequence. Layers of each element were deposited on the substrate in the order of $(Ti\text{-}Se)_m$-$(Bi\text{-}Se)_m$ where m = 1, 2, and 3 and each sequence was repeated to obtain a total film thickness of approximately 50 nm. The composition and thicknesses of the Ti-Se and Bi-Se were calibrated as describe in detail by Atkins *et. al.* as well as briefly below.[40] Samples on the silicon were annealed at specified temperatures for 30 minutes in a nitrogen atmosphere with oxygen below 1.0 ppm. Electron-probe microanalysis (EPMA) was used to determine the composition of the thin film samples on silicon.[41]

Freestanding films for calorimetry measurements were prepared from the films deposited on the PMMA coated substrates by dissolving the PMMA using acetone and filtering out the film particles using a Teflon filter. Differential scanning calorimetry (DSC) data was collected on a Netzsch STA 409 PC Luxx thermal analyzer using 1-3 mg of freestanding film, which were placed into an aluminum pan and sealed by crimping. Samples were heated from ambient temperatures to 400 °C at rates of 15 °C/min under a flow of nitrogen and then cooled back to room temperature. Without

disturbing the sample or instrument, this cycle was repeated to measure reversible transitions in the sample as well as the cell background. The net heat flow, associated with the irreversible changes occurring in the sample during the initial heating cycle, was determined by subtracting the data collected during the second cycle from those for the first. To check for reproducibility in the cell background a third cycle was collected and compared to the second cycle.

X-ray reflectivity (XRR) and specular X-ray diffraction (XRD) patterns were measured on a Bruker D8 Discover diffractometer with Cu-Kα radiation, equipped with a Göbel mirror. Grazing incidence in-plane X-ray diffraction patterns were acquired on a Rigaku Smartlab (Cu Kα) diffractometer and on the Multi-Purpose General Scattering beamline 33-BM-C (λ = 1.2653 Å) at the Advanced Photon Source (APS), at Argonne National Laboratory. X-ray fluorescence measurements were performed on a Rigaku ZSX Primus-II with a Rhodium X-ray source. For the $m = 1$ compound the c-axis lattice parameters were calculated using modified Braggs' law. Least-squares fits of the in-plane lattice parameters (a and b) of $TiSe_2$ and BiSe were done using the WinCSD software package.[42] In-plane lattice parameters (a and b) of $TiSe_2$ and BiSe and the c-axis lattice parameters were refined using Full pattern Le Bail fits done in the FullProf Suite.[43–45]

Scanning transmission electron microscopy (STEM) cross-sections were prepared on an FEI Helios 600-Dual Beam focused ion beam (FIB) with a side winder ion column using backside milling methods[46] and wedge pre-milling methods.[47] High angle annular dark field scanning transmission electron microscopy (HAADF-STEM) was performed on a FEI Titan 80-300 TEM/STEM at 300 keV.

Results and Discussion

Layered precursors were prepared with compositional modulation that mimics the target compounds, $[(BiSe)_{1+\delta}]_m[TiSe_2]_m$ m = 1, 2, and 3. A calibration procedure was used to determine the deposition parameters (local compositions, layer thicknesses, and layer sequences) required to crystallize the desired products.[40] Briefly, the ratio of the elements in binary Bi-Se and Ti-Se multilayer films were calibrated by keeping the amount of Se constant in each bilayer and varying the thickness of the metal. The thickness and atomic composition were determined via XRR and EPMA, respectively, and the ratio of the deposition thicknesses were chosen to match the 1:1 stoichiometry of BiSe and the 1:2 stoichiometry of $TiSe_2$. The ratio of Bi/Ti was adjusted to match the misfit (1.15) of the previously reported $(BiSe)_{1.15}TiSe_2$ compound[39] by preparing samples with a Bi-Se-Ti-Se sequence that held the metal to Se ratios in each layer constant and varied the thickness of one of the constituent layers. XRR and EPMA were used to determine the deposition parameters required to obtain the desired misfit. The thicknesses of the $(Bi\text{-}Se)_1$ and $(Ti\text{-}Se)_1$ bilayers were adjusted to correct the absolute thickness to yield one layer of BiSe and one layer of $TiSe_2$ as determined by the quality of the diffraction pattern of $[(BiSe)_{1+\delta}]_1[TiSe_2]_1$ which self-assembled on annealing. To prepare precursors designed to form the m = 2 and 3 compounds, the layer sequences Bi-Se-Bi-Se-Ti-Se-Ti-Se and Bi-Se-Bi-Se-Bi-Se-Ti-Se-Ti-Se-Ti-Se were deposited using the deposition parameters of the m = 1 compound until films of approximately 50 nm were obtained.

To characterize the evolution of the super-structure and individual constituent structures upon heating the $(BiSe)_1$-$(TiSe_2)_1$ precursor, specular (Figure 2.1a) and in-

plane (Figure 2.1b) X-ray diffraction were collected. At low annealing temperatures, the specular scan has intensity maxima from two sources. At small Q values there are sharp reflections from the periodic modulation of the electron density resulting from the sequential deposition of the elements. At larger Q values, there are broader maxima due to the crystallization of the constituents.[48] The first reflection yields a *c*-axis lattice parameter that is approximately 0.08 Å smaller than the *c*-axis lattice parameter corresponding to the higher order reflections. For annealing temperatures between 150°C and 250°C, diffusion results in growth of the targeted $[(BiSe)_{1+\delta}]_1[TiSe_2]_1$ product, and the reflections due to the artificial modulation gradually shift to positions corresponding to a single family of 00*l* reflections. Concurrently, the broader maxima sharpen and gain intensity, and additional reflections are resolved, indicating the BiSe and $TiSe_2$ layers become more coherent with one another. The *c*-axis lattice parameter decreases between annealing temperatures of 150 °C and 250 °C, consistent with atoms diffusing to form atomic planes expected for the BiSe and $TiSe_2$ structures. Above 250 °C the *c*-axis lattice parameter remains constant, within error. Lattice parameters are summarized in Table 1 and are consistent with those previously reported.[39]

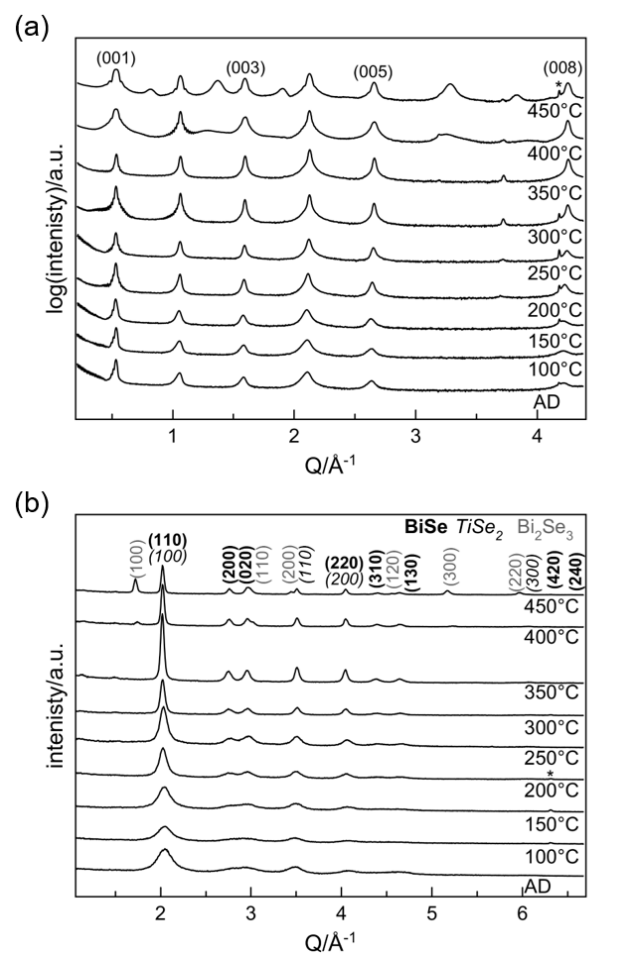

Figure 2.1: (a) Specular and (b) in-plane X-ray diffraction patterns for a $(Ti\text{-}Se)_1$-$(Bi\text{-}Se)_1$ precursor after annealing at each temperature for 30 minutes.

The in-plane diffraction data provides information on the structures of the constituent layers in the compound. All reflections can be indexed as *hk*0 reflections of either BiSe or $TiSe_2$, with no observable Bi_2Se_3 reflections until after annealing at 400 °C. The scan of the as-deposited precursor contains broad reflections characteristic of small grains for both BiSe and $TiSe_2$. When comparing the $TiSe_2$ (110) and BiSe (200) reflections in the as-deposited film, greater relative intensity and narrower line width is initially observed for the $TiSe_2$ reflections, indicating that more crystalline $TiSe_2$ forms during deposition relative to BiSe. As the annealing temperature is increased, the intensity of the in-plane reflections for both BiSe and $TiSe_2$ increase. The splitting of

the BiSe reflection, at approximately 3 $Å^{-1}$, indicates that the in-plane unit cell is rectangular, and the increase in the splitting with increasing annealing temperature indicates that the difference between the *a*- and *b*-axis lattice parameters increases. The in-plane areas of both constituents increase slightly as the annealing temperature is increased.

Table 2.1: Lattice parameters for $(Ti\text{-}Se)_1\text{-}(Bi\text{-}Se)_1$ precursor after annealing for 30 minutes at various temperatures.

Annealing Temp (°C)	*c* (Å)	BiSe a (Å)	BiSe *b* (Å)	$TiSe_2$ *a* (Å)
AD	11.94(2)	4.52(1)	4.23(1)	3.56(2)
100	11.94(2)	4.54(2)	4.25(2)	3.56(2)
150	11.94(2)	4.521(8)	4.238(7)	3.59(1)
200	11.894(8)	4.547(4)	4.244(3)	3.587(4)
250	11.84(1)	4.533(4)	4.234(3)	3580(5)
300	11.821(4)	4.557(2)	4.242(1)	3.579(2)
350	11.81(2)	4.564(2)	4.246(1)	3.580(3)
400	11.83(2)	4.551(2)	4.244(1)	3.589(3)
450	11.822(4)	4.548(1)	4.251(1)	3.583(1)

After annealing at 450 °C, additional reflections are observed in both the specular and in-plane diffraction patterns that indicate that an impurity phase of Bi_2Se_3, which is crystallographically aligned to the substrate, forms. When comparing X-ray fluorescence measurements collected after annealing at 450°C and 300°C, a ~40% decrease in Se counts and a significant increase in integrated O counts was observed, without significant changes in the Bi or Ti intensities. If all the $TiSe_2$ was converted to TiO_2, one would expect a 63.5% decrease in Se counts, assuming a misfit of 1.15. This suggests that the Bi_2Se_3 results from partial destruction of the superlattice as $TiSe_2$ is convert to TiO_2, which is consistent with the decrease in the in-plane intensity of $TiSe_2$ reflections after annealing at 450°C. The TiO_2 is not observed in the diffraction pattern

either because it is amorphous or because the grain sizes are too small to be observed relative to the other, crystallographically aligned compounds. A balanced chemical equation for this conversion is:

$$2[(BiSe)_{1+\delta}]_1[TiSe_2]_1 + 2O_2 \rightarrow (1+\delta)\ Bi_2Se_3 + 2TiO_2 + (3-\delta)\ Se$$

where bismuth and selenium are being oxidized. Some of the selenium that is not reacted to form Bi_2Se_3 could be further oxidized to form SeO_2.

An annealing study was performed on the $(Ti\text{-}Se)_2\text{-}(Bi\text{-}Se)_2$ precursor (Figure 2.2) to ascertain the conditions required to crystallize $[(BiSe)_{1+\delta}]_2[TiSe_2]_2$. As found in the precursor for $[(BiSe)_{1+\delta}]_1[TiSe_2]_1$, the specular scan of the as-deposited precursor (Figure 2.2a) contains relatively sharp and intense maxima at small Q resulting from the periodic modulation of the electron density produced by the precursor deposition. At larger Q values, broader maxima are present consistent with the formation of small domains of the targeted $[(BiSe)_{1+\delta}]_2[TiSe_2]_2$ compound. The in-plane diffraction scan of the as-deposited precursor contains broad, low intensity reflections that are consistent with small amounts of crystalline BiSe and $TiSe_2$. As annealing temperature is increased, reflections at larger Q values grow in intensity in the specular scan. The reflections from the initial elemental modulation shift as annealing temperature increases, such that by 250°C all of the specular reflections approach that expected fr0m a single family of 00*l* reflections. The superlattice is aligned to the substrate with a *c*-axis lattice parameter of 23.792(2) Å determined from the large Q reflections. The intensity of the reflections for BiSe and $TiSe_2$ in the in-plane diffraction scans also increase as annealing temperature is increased. The growth of BiSe and $TiSe_2$ as well as the observed superlattice reflections are consistent with the formation of the targeted

$[(BiSe)_{1+\delta}]_2[TiSe_2]_2$ compound. Annealing at 250°C results in the largest intensities of the reflections attributed to $[(BiSe)_{1+\delta}]_2[TiSe_2]_2$ in both the specular and in-plane diffraction scans. This is the first data that suggests that BiSe layers thicker than one bilayer can be formed in heterostructures.

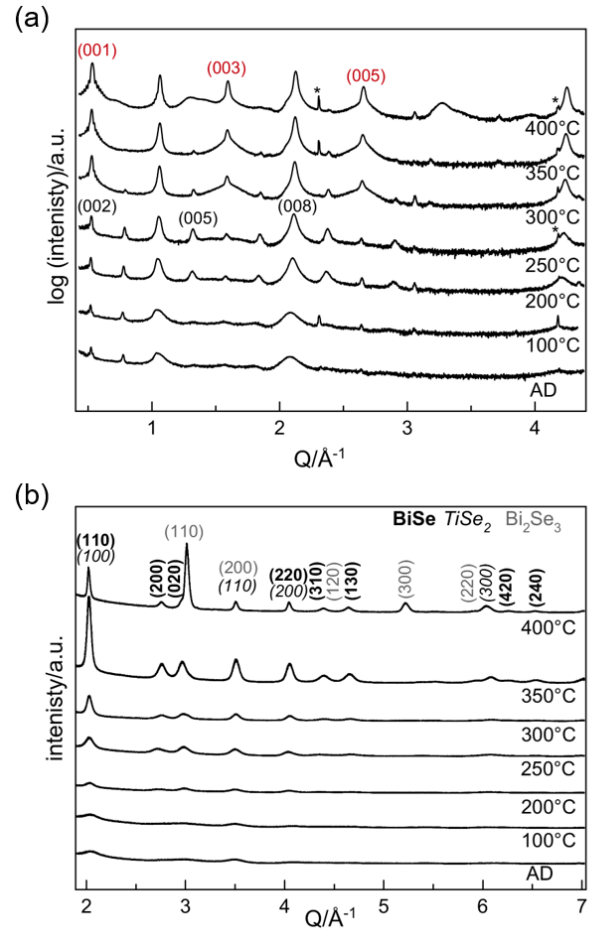

Figure 2.2: (a) Specular and (b) in-plane X-ray diffraction patterns for a $(Ti\text{-}Se)_2$-$(Bi\text{-}Se)_2$ precursor after annealing at each temperature for 30 minutes.

Annealing at 300 and 350°C results in changes to the diffraction patterns that indicates that $[(BiSe)_{1+\delta}]_2[TiSe_2]_2$ transforms into $[(BiSe)_{1+\delta}]_1[TiSe_2]_1$. At 300 °C, the intensity of odd order 00*l* reflections in the specular diffraction pattern decay while the even 00*l* reflections become more intense. Despite these changes, the in-plane pattern

contains only *hk*0 reflections from BiSe and $TiSe_2$, suggesting that the $m = 2$ superstructure is decomposing into $[(BiSe)_{1+\delta}]_1[TiSe_2]_1$. By 350 °C, the 00*l* reflections solely from $[(BiSe)_{1+\delta}]_2[TiSe_2]_2$ are nearly absent and the remaining reflections can be indexed to the $[(BiSe)_{1+\delta}]_1[TiSe_2]_1$ superstructure. $[(BiSe)_{1+\delta}]_2[TiSe_2]_2$ is only kinetically stable as it decomposes at elevated annealing temperatures into $[(BiSe)_{1+\delta}]_1[TiSe_2]_1$.

Table 2 summarizes the changes in the lattice parameters corresponding to the targeted $[(BiSe)_{1+\delta}]_2[TiSe_2]_2$ compound after each annealing temperature. The c-axis lattice parameter decreases as annealing temperature increases, reflecting increased order as the atoms arrange to form $[(BiSe)_{1+\delta}]_2[TiSe_2]_2$. Annealing at temperatures greater than 200 °C causes the difference between the BiSe *a* and *b* in-plane lattice parameters to decrease, however there is an insignificant change in the in-plane area. Annealing at 300 °C and above results in the in-plane lattice parameters of both constituents converging toward the lattice parameters of $[(BiSe)_{1+\delta}]_1[TiSe_2]_1$. This is consistent with the evolution of the specular diffraction pattern and supports the hypothesis that the targeted $[(BiSe)_{1+\delta}]_2[TiSe_2]_2$ compound decomposes into $[(BiSe)_{1+\delta}]_1[TiSe_2]_1$ (indices shown in red in figure 2.2a). At 400 °C, reflections in both the specular and in-plane diffraction patterns indicate that Bi_2Se_3 is present. This is consistent with the data presented on the annealing of $[(BiSe)_{1+\delta}]_1[TiSe_2]_1$, which clearly shows that at these elevated temperatures, $[(BiSe)_{1+\delta}]_1[TiSe_2]_1$ reacts with oxygen and releases Se^{-2} ions that react with the BiSe layers to form Bi_2Se_3. The small difference in the $TiSe_2$ lattice parameters of $[(BiSe)_{1+\delta}]_1[TiSe_2]_1$ formed through decomposition ($a = 3.604(5)$) and $[(BiSe)_{1+\delta}]_1[TiSe_2]_1$ formed from a designed precursor

(a = 3.580(3)) may reflect differences in composition due to defects and/or the concentration of anti-phase boundaries in the BiSe layer.

Table 2.2: Lattice parameters for $(Ti\text{-}Se)_2$-$(Bi\text{-}Se)_2$ precursor after annealing at each temperature for 30 minutes.

Annealing Temp (°C)	c (Å)	BiSe a (Å)	BiSe b (Å)	$TiSe_2$ a (Å)
AD	24.08(1)	4.55(3)	4.23(2)	3.56(1)
100	24.06(1)	4.51(1)	4.22(1)	3.59(1)
200	23.991(2)	4.597(6)	4.222(4)	3.591(3)
250	23.792(2)	4.581(6)	4.230(5)	3.587(1)
300	23.725(1)	4.562(4)	4.233(3)	3.577(1)
350	23.689(1)	4.558(2)	4.240(2)	3.579(1)
400	-	4.558(1)	4.250(1)	3.604(5)

Specular (Figure 2.3a) and in-plane (Figure 2.3b) diffraction scans were also collected after annealing the $(Ti\text{-}Se)_3$-$(Bi\text{-}Se)_3$ precursor at various temperatures. Like the previously discussed precursors, the as-deposited specular diffraction scan contains small Q diffraction maxima from the designed compositional modulation and broad Bragg reflections at larger Q indicating some long-range order due to self-assembly during deposition. The as-deposited in-plane diffraction scan contains reflections expected for BiSe and $TiSe_2$, and weak reflections that are consistent with the presence of a small amount of Bi_2Se_3. Below 200°C, there are only slight increases in both in-plane lattice parameters of BiSe and a decrease in the a-axis lattice parameter of $TiSe_2$ (Table 3), suggesting that there is little interdiffusion and/or self-assembly occurring.

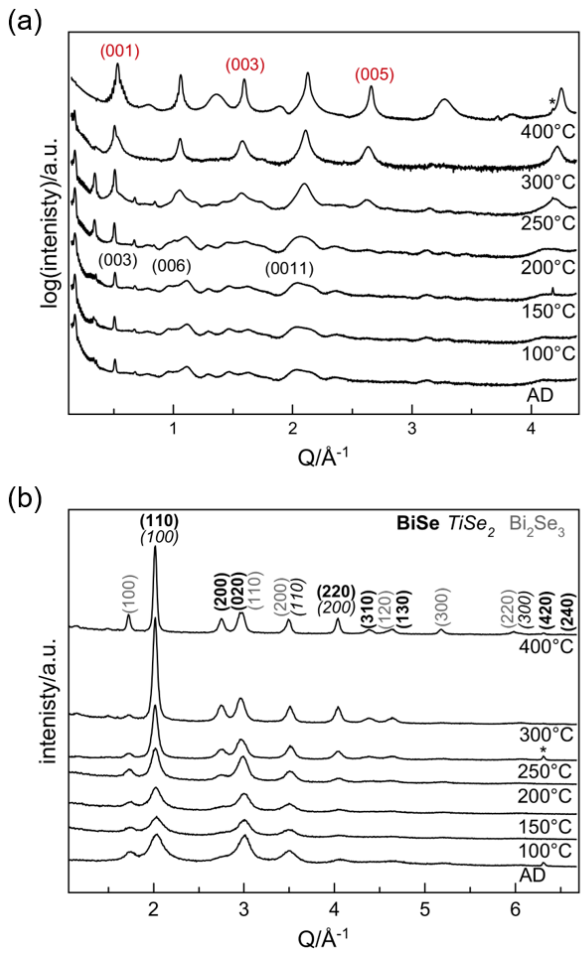

Figure 2.3: (a) Specular and (b) in-plane X-ray diffraction patterns for a $(Ti\text{-}Se)_3$-$(Bi\text{-}Se)_3$ precursor after annealing at each temperature for 30 minutes.

At 200°C and above, there are significant changes to the structure of the $(Ti\text{-}Se)_3$-$(Bi\text{-}Se)_3$ precursor. In the 200°C specular scans, a series of reflections appear at low Q values, consistent with a repeat spacing of 37.2(2) Å. The reflection at approximately 2.1 $Å^{-1}$ changes from two overlapped reflections at lower temperatures to a broad reflection at 200°C. The reflections at higher Q values are not consistent with the reflections at low Q values, yielding a repeat spacing of 34.3(2) Å. At 250°C the intensity of reflections in the specular diffraction scan expected for $[(BiSe)_{1+\delta}]_1[TiSe_2]_1$ grow in intensity, an additional reflection grows in at low Q, and the higher Q reflections do not change in intensity. At 300°C the specular diffraction pattern is

consistent with that expected for $[(BiSe)_{1+\delta}]_1[TiSe_2]_1$. The in-plane diffraction patterns show only growth of *hk*0 reflections for BiSe and $TiSe_2$ when annealed at temperature of 300°C and below. The evolution of the $(Ti\text{-}Se)_3$-$(Bi\text{-}Se)_3$ precursor at lower temperatures is more complex than observed for the $(Ti\text{-}Se)_2$-$(Bi\text{-}Se)_2$ precursor, but it also evolves into $[(BiSe)_{1+\delta}]_1[TiSe_2]_1$ after annealing at 300°C. At 400°C, reflections for Bi_2Se_3 appear in the specular scan and the intensity of the Bi_2Se_3 reflections in the in-plane scan become much more intense. This is consistent with the oxidation of $[(BiSe)_{1+\delta}]_1[TiSe_2]_1$ discussed previously.

Table 2.3: Lattice parameters for $(Ti\text{-}Se)_3$-$(Bi\text{-}Se)_3$ precursor after annealing at each temperature for 30 minutes.

Annealing Temp (°C)	BiSe *a* (Å)	BiSe *b* (Å)	$TiSe_2$ *a* (Å)
AD	4.50(1)	4.23(1)	3.616(2)
100	4.46(2)	4.23(1)	3.592(3)
150	4.54(1)	4.25(1)	3.583(2)
200	4.557(3)	4.258(3)	3.576(1)
250	4.547(2)	4.242(2)	3.567(1)
300	4.553(1)	4.240(1)	3.575(1)
400	4.564(1)	4.255(1)	3.597(1)

Figure 2.4 shows a comparison of the specular and in-plane diffraction patterns of the $(Ti\text{-}Se)_1|(Bi\text{-}Se)_1$, $(Ti\text{-}Se)_2|(Bi\text{-}Se)_2$ and $(Ti\text{-}Se)_3|(Bi\text{-}Se)_3$ precursors annealed at their optimum temperatures to form their targeted compound. The diffraction pattern of the annealed $(Ti\text{-}Se)_1|(Bi\text{-}Se)_1$ precursor contains sharp, defined reflections in both specular and in-plane geometries, indicating that the compound $[(BiSe)_{1+\delta}]_1[TiSe_2]_1$ has formed with a high degree of crystallinity. The *c*-axis lattice parameter obtained from the diffraction pattern, 11.81(2) Å, is slightly larger than that reported previously (11.77 Å).[39] The specular diffraction pattern of the annealed $(Ti\text{-}Se)_2|(Bi\text{-}Se)_2$ precursor is

consistent with the formation of the targeted $[(BiSe)_{1+\delta}]_2[TiSe_2]_2$ compound, however the low Q reflections are shifted to slightly lower angles than expected from the positions of the higher Q reflections. This reflects contributions to the intensity from the artificial layering of the precursor resulting in a *c*-axis of 24.06(3) Å calculated from the first 3 reflections.[48] The remaining, higher Q, reflections yield a *c*-axis of 23.79(2) Å as they are dominated by intensity from the crystalline compound. The *c*-axis lattice parameter of the crystalline compound is about 0.2 Å greater than twice the *c*–axis lattice parameter of $[(BiSe)_{1+\delta}]_1[TiSe_2]_1$. This difference results from the different interfaces present in the two materials and implies that the BiSe-BiSe bilayer spacings or the $TiSe_2$-$TiSe_2$ van der Waals gap are larger than the BiSe-$TiSe_2$ van der Waals gap.[49,50] This may suggest that greater attractive forces exist between BiSe-$TiSe_2$ interfaces compared to the BiSe-BiSe or $TiSe_2$-$TiSe_2$ interfaces, which provides a rationale as to why the compounds become increasingly unstable as the relative number of BiSe-$TiSe_2$ interfaces are decreased. The specular diffraction pattern of the annealed $(Ti\text{-}Se)_3|(Bi\text{-}Se)_3$ precursor contains reflections from two sources. The sharp, defined reflections at small Q values that grow in intensity during annealing yield a repeating thickness of 37.2(2) Å. The broader reflections at larger Q values can be indexed as a single family of reflections, yielding a *c*-axis lattice parameter of 34.3(2) Å. Since the difference between the lattice parameters of $[(BiSe)_{1+\delta}]_2[TiSe_2]_2$ and $[(BiSe)_{1+\delta}]_1[TiSe_2]_1$ is 12 Å, an estimate for the expected lattice parameter of $[(BiSe)_{1+\delta}]_3[TiSe_2]_3$ is ~ 36.3 Å. which is between these two values. This suggests that, at best, there is only partial self-assembly of the targeted $[(BiSe)_{1+\delta}]_3[TiSe_2]_3$ compound.

The reflections present in the in-plane diffraction scan of the annealed samples support this interpretation of the specular diffraction patterns. The reflections in the in-lane diffraction pattern of $[(BiSe)_{1+\delta}]_1[TiSe_2]_1$ are sharper than those present in $[(BiSe)_{1+\delta}]_2[TiSe_2]_2$ and all reflections in patterns collected at 300°C or less can be indexed as either BiSe or $TiSe_2$ reflections. The BiSe reflections in the in-plane diffraction pattern of the annealed $(Ti\text{-}Se)_3|(Bi\text{-}Se)_3$ precursor are less defined and broader than those in the other compounds. This data suggests that the $[(BiSe)_{1+\delta}]_2[TiSe_2]_2$ compound is less crystalline than $[(BiSe)_{1+\delta}]_1[TiSe_2]_1$, and the $[(BiSe)_{1+\delta}]_3[TiSe_2]_3$ compound is even less well crystalized, highlighting the difficulty of synthesizing these kinetically stable compounds.

The stability difference between the three compounds can be understood through a simple parallel plate capacitor model. Assuming complete charge donation of one electron per BiSe bilayer to the $TiSe_2$, one could calculate the stabilization energy due to the ionic attraction between the layers using the following equation, $V_m = 1/(4\pi\varepsilon_m)(-m^2e^2/r_m)$, where ε_m is the permittivity of the material between the layers, e is the elementary charge, me is the charge of the layers and r_m is the distance between the charges. For $m = 1$, we assume that r_1 is the distance between the BiSe and $TiSe_2$ layers and ε_1 is the permittivity of the van der Waals gap. If charge is concentrated at the surface of the layers, so r_m remains the distance between the BiSe and $TiSe_2$ layers, as m is increased one would expect greater stability for $[(BiSe)_{1+\delta}]_m[TiSe_2]_m$ relative to m $[(BiSe)_{1+\delta}]_1[TiSe_2]_1$ layers because the stabilization energy increases as m^2. However, because BiSe is a semiconductor and $TiSe_2$ is a small band gap semiconductor or a semi metal (dependent on defect concentration) a space charge region will form at the

interface on the two materials. The separation of the charges will be larger than the distance between the BiSe - $TiSe_2$ van der Waals gap. If the *c*-axis lattice parameter is smaller than the charge depletion width, then the separation between the charges scales with the *c*-axis lattice parameter. Since the *c*-axis lattice parameter is proportional to *m*, r_m is proportional to mr_1. As the depletion width grows, the dielectric constant separating the charges is that of the van der Waals gap plus a portion of the layers themselves. This results in a larger value for the permittivity, $\varepsilon_m > \varepsilon_1$ and leads to less stabilization for $[(BiSe)_{1+\delta}]_m[TiSe_2]_m$ relative to *m* $[(BiSe)_{1+\delta}]_1[TiSe_2]_1$ layers.

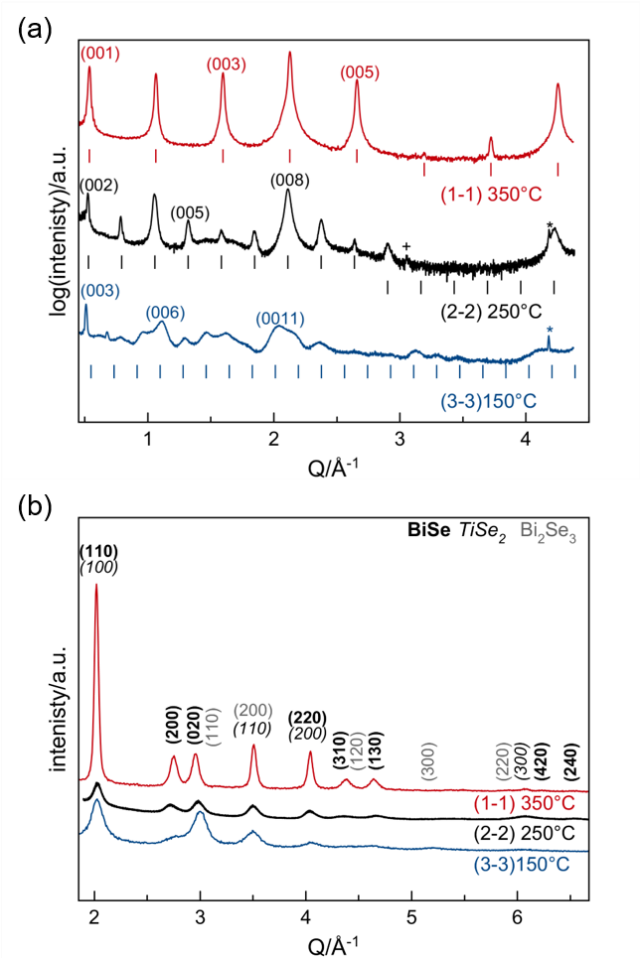

Figure 2.4: (a) Specular and (b) in-plane X-ray diffraction patterns for $[(BiSe)_{1+\delta}]_2[TiSe_2]_2$ and $[(BiSe)_{1+\delta}]_3[TiSe_2]_3$ compounds prior to evidence of decomposition are compared to the $[(BiSe)_{1+\delta}]_1[TiSe_2]_1$ compound after annealing each to the listed temperature for 30 minutes. Tick marks are added to (a) as a visual aid of the location of the reflections from the calculated lattice parameters.

Cross-sectional HAADF-STEM images of the $(Ti\text{-}Se)_2|(Bi\text{-}Se)_2$ precursor annealed at pre- and post- decomposition temperatures were collected to gain information about the local structure and the structural rearrangements that occurs with decomposition. Figure 2.5 shows a representative HAADF-STEM image of the $[(BiSe)_{1+\delta}]_2[TiSe_2]_2$ precursor annealed at 250 °C, the temperature where the compound is best formed. The image indicates that the average structure is comprised of two BiSe bilayers alternating with two $TiSe_2$ layers, however the sample contains many defects.

Numerous substitutional defects are present, where part of a BiSe layer is replaced by a $TiSe_2$ layer and vice versa. The average period estimated from this image is consistent with the c-axis lattice parameter of the superlattice, calculated from the specular diffraction. Where visible, the zone axis orientations differ in each layer, which is consistent with the turbostratic disorder observed previously in $(BiSe)_{1.15}TiSe_2$ prepared via the same self-assembly approach.[39,51] Where a $TiSe_2$ (110) zone axis is visible, it is clear that $TiSe_2$ is a 1T polytype. The different zone axis orientations of the BiSe layer are consistent with a distorted rock salt structure. When the BiSe layer is orientated along a (110) zone axis, so called antiphase boundaries can be found, where two Bi atoms are adjacent to one another.[52] The limited spatial extent of the zone axis domains indicates the layers are comprised of many small grains, which is consistent with the broad reflections observed in the in-plane diffraction.

Figure 2.6 contains a representative HAADF-STEM of the $(Ti\text{-}Se)_2|(Bi\text{-}Se)_2$ precursor annealed at 400 °C. The image contains two distinct regions, one containing $[(BiSe)_{1+\delta}]_1[TiSe_2]_1$ and the other Bi_2Se_3 resulting from the reaction of $[(BiSe)_{1+\delta}]_1[TiSe_2]_1$ with oxygen. During the rearrangement of $[(BiSe)_{1+\delta}]_2[TiSe_2]_2$ to $[(BiSe)_{1+\delta}]_1[TiSe_2]_1$, atoms must diffuse perpendicular to the layering. The Bi_2Se_3 phase is segregated to the surface of the film as reaction with oxygen is likely a gas-solid reaction. The Bi_2Se_3 has a preferred alignment with respect to the substrate, in agreement with the diffraction data. The $[(BiSe)_{1+\delta}]_1[TiSe_2]_1$ is under the Bi_2Se_3, and the interfaces between the BiSe and $TiSe_2$ layers are atomically smooth. The $[(BiSe)_{1+\delta}]_1[TiSe_2]_1$ region is remarkably defect free considering the low annealing temperature and short annealing times required to transform from $[(BiSe)_{1+\delta}]_2[TiSe_2]_2$.

Antiphase boundaries are present in the BiSe layer, as reported previously.[51,53,54] The visible zone axis change orientations layer to layer, consistent with turbostratic disorder. The Bi_2Se_3 region contains more defects, including regions where it appears that BiSe monolayers separate Bi_2Se_3 layers. These defects likely result from the non-stoichiometry resulting from the disproportionation of the $(Ti\text{-}Se)_2|(Bi\text{-}Se)_2$ precursor.

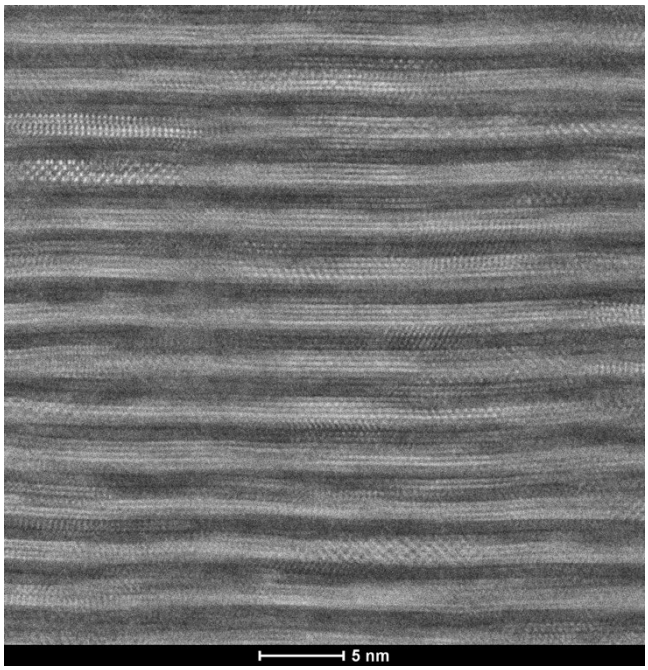

Figure 2.5: Cross-sectional HAADF-STEM image of the $(Ti\text{-}Se)_2|(Bi\text{-}Se)_2$ precursor annealed to 250°C. The gray scale contrast differentiates the different atomic species, with the Bi containing regions appearing bright compared to the darker regions that contain Ti atoms.

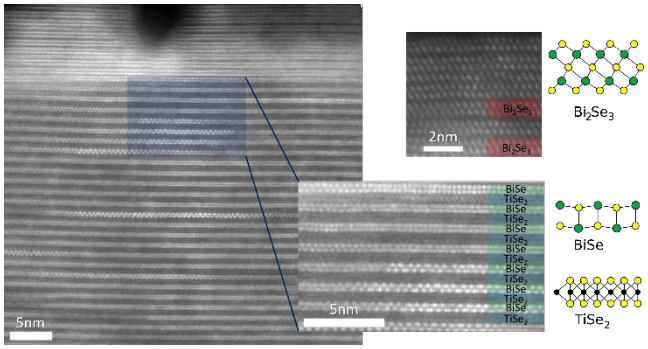

Figure 2.6: Cross-sectional HAADF-STEM image of the $(Ti\text{-}Se)_2|(Bi\text{-}Se)_2$ precursor annealed to 400°C. The sample is predominately $[(BiSe)_{1+\delta}]_1[TiSe_2]_1$ (inset, bottom), capped by textured Bi_2Se_3 (inset, top).

DSC data was collected on the three $(Ti\text{-}Se)_m|(Bi\text{-}Se)_m$ precursors to further probe the formation and subsequent decomposition with increased annealing temperature (Figure 2.7). The DSC scan of the $(Ti\text{-}Se)_1|(Bi\text{-}Se)_1$ precursor contains a broad exotherm that starts at approximately 125 °C, an endotherm at approximately 220

°C, and a second broad exotherm with a maximum heat flow at approximately 375°C. The sharp endotherm at 220°C is from the melting of Se in the precursor. The exotherm at 375°C is the oxidation of the sample. The DSC scan of the $(Ti\text{-}Se)_2$-$(Bi\text{-}Se)_2$ precursor contains two broad exotherms, with one maximum heat flow at approximately 125°C and the second at approximately 300 °C. The diffraction data collected as a function of annealing suggests that the low temperature exotherm results from the formation of the $[(BiSe)_{1+\delta}]_2[TiSe_2]_2$. The HAADF-STEM and diffraction data suggests that the higher temperature exotherm results from the transformation of $[(BiSe)_{1+\delta}]_2[TiSe_2]_2$ into $[(BiSe)_{1+\delta}]_1[TiSe_2]_1$. The high temperature shoulder on this exotherm is the oxidation of $[(BiSe)_{1+\delta}]_1[TiSe_2]_1$ and correlates with the appearance of Bi_2Se_3 in the X-ray diffraction annealing study. The scan of the $(Ti\text{-}Se)_3$-$(Bi\text{-}Se)_3$ precursor contains a low temperature exotherm with a maximum heat flow at approximately 125°C and a second higher temperature exotherm with a maximum heat flow at approximately 350 °C. The diffraction data suggests that the smaller low temperature exotherm results from partial self-assembly of the targeted $[(BiSe)_{1+\delta}]_3[TiSe_2]_3$ compound and that the higher temperature exotherm results from the transformation into $[(BiSe)_{1+\delta}]_1[TiSe_2]_1$.

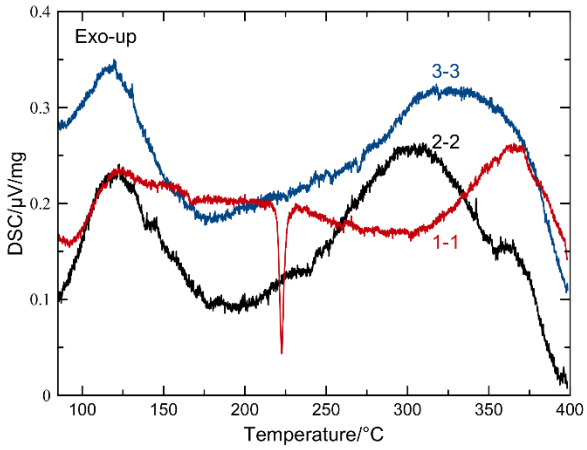

Figure 2.7: Differential scanning calorimetry data for the 1-1 (red), 2-2 (black), and 3-3 (blue) as-deposited precursor.

The results presented in this manuscript suggests that BiSe-$TiSe_2$ containing heterostructures exist in local free energy minima as depicted in Figure 2.8 with a qualitative schematic of the structures. The compounds become increasingly less stable as m, the thickness of the constituent layers, is increased. This corresponds to the decreasing depth of the free energy minima as m increases in Figure 2.8. When given sufficient energy to overcome the activation barrier associated with solid-state diffusion, the compounds lower their energy by rearranging into $[(BiSe)_{1+\delta}]_1[TiSe_2]_1$, which is the global minimum within this restricted energy landscape. The formation of Bi_2Se_3 as a secondary phase in the annealing experiments suggests that intergrowths containing Bi_2Se_3 with $TiSe_2$ and/or BiSe may be possible under the correct synthesis conditions from appropriately designed precursors.

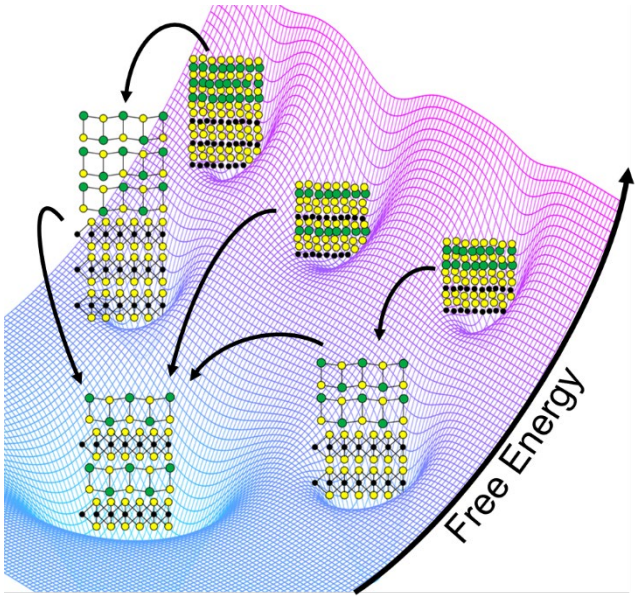

Figure 2.8: Schematic free energy landscape. The 2-2 and 3-3 compounds exist in shallower local minima than the 1-1 compound and can lower their free energy by rearranging into the 1-1 structure. Arrows indicate transitions from higher energy states (shallower wells) to lower energy states (deeper wells). The schematic images of the as-deposited layers do not depict the small percentage of the films that have already begun to self-assemble into the ordered layers.

Conclusion

Here we report the synthesis of kinetically stable BiSe-$TiSe_2$ containing heterostructures, $[(BiSe)_{1+\delta}]_m[TiSe_2]_m$ for $m \leq 3$. Specular X-ray diffraction, collected after annealing at various temperatures, revealed the formation and subsequent decomposing of the targeted superlattices. The m = 2 and 3 compounds decomposed into $[(BiSe)_{1+\delta}]_1[TiSe_2]_1$. At higher temperatures $[(BiSe)_{1+\delta}]_1[TiSe_2]_1$ reacts with traces of oxygen, forming Bi_2Se_3 on the surface. The compounds become increasingly unstable as m is increased. These results demonstrate that kinetically stable compounds exist in a complex free energy landscape defined by the interactions within and between the constituents. While many members of a homologous series of compounds can be

imagined, the complex free energy landscape governs which compounds can be formed and highlights the difficulty of synthesizing multiple members of a potential homologous series of compounds, especially those with identical stoichiometry. The results of this manuscript demonstrate that chemists can gain valuable qualitative knowledge of the free energy landscape through studies of precursors designed to produce different members of a homologous series.

Chapter 3: Synthesis, Structure, and Properties of Three Constituent Heterostructure $(BiSe)_{1+\delta}(Bi_2Se_3)_{1+\gamma}(BiSe)_{1+\delta}TiSe_2$

Introduction

As potentially applicable in high-performance electronics and quantum computers, topological insulators and heterostructures containing them have recently garnered significant interest by materials scientists.[55–59] Despite their imagined utility, these compounds have proven difficult to synthesize. Typically, heterostructures are prepared by mechanical assembly of exfoliated few or monolayer flakes of desired materials. However, this method is limited to materials that are stable as isolated monolayers. Direct synthesis methods such as molecular beam epitaxy (MBE) and chemical vapor deposition (CVD) have successfully grown heterostructures containing constituents that are not stable as isolated monolayers or cannot be derived from bulk compounds.[60–62] Unfortunately, MBE favors a lattice match between the constituents, CVD requires a carful choice of reactive precursors and both methods generally use high processing tempertures.[7] These factors limit the number of potential new compounds that can be prepared since high processing temperature typically yield thermodynamic products. Thus, synthesis methods utilizing elemental precursors and kinetically-limited reactions, such as the modulated elemental reactants (MER) method, are favorable for exploratory synthesis of new heterostructures containing topological insulators.

Recently we reported the formation and subsequent decomposition of kinetically formed metastable compounds $[BiSe_{1+\delta}]_m[TiSe_2]_m$ with m = 1, 2, 3.[63] When the m = 3

compound decomposed, new reflections in the specular diffraction pattern suggested that a heterostructure with a smaller unit cell began to form before it too decomposed to the $m = 1$ compound. Additionally, for the $m = 3$ it was observed that the topological insulator Bi_2Se_3 formed upon deposition and was present at all annealing temperatures.[63] Bi_2Se_3 is of considerable interest because it is an extensively studied topological insulator, with a robust single Dirac cone, thickness dependent band structure, and defect induced band bending.[64–66] Additionally, Bi_2Se_3 is one member of the Bi_xSe_y family of compounds that form an "infinitely adaptive series".[67] Compounds in this series are comprised of stacks of Bi_2Se_3 quintuple-layers and Bi bilayers, of various thicknesses, separated by van der Waals gaps. We speculate that the new heterostructure observed in the $m = 3$ compound may consist of one member in the Bi_xSe_y series interleaved with $TiSe_2$ and BiSe. To test if the new heterostructure incorporating Bi_xSe_y could be synthesized, a series of $(Bi\text{-}Se)_3\text{-}TiSe_2$ precursors with varying Bi-Se ratios and layer thickness were prepared and annealed at various temperatures for 30 minutes. The result was studied using X-ray diffraction.

Experimental

Amorphous layered precursors were simultaneously deposited on ambient temperature silicon and quartz substrates using a custom-build physical vapor deposition system. A shadow mask was used on the quartz substrates to produce a cross geometry for electrical measurements. Element Ti and Bi were deposited using electron beam guns and elemental Se was-deposited using an effusion cell. The rate of deposition of each element was independently monitored *in situ* using quartz crystal microbalances. Computer-controlled pneumatic shutters placed above each source

regulated the deposition sequence and thicknesses. Samples were annealed on a hot plate between 100-450 °C in a nitrogen atmosphere with less than 1 ppm oxygen.

X-ray diffraction was collected on a Bruker D8 Discover diffractometer (Cu Kα) equipped with a Göbel mirror. Grazing incidence in-plane X-ray diffraction patterns were acquired on a Rigaku Smartlab (Cu Kα) diffractometer. X-ray fluorescence measurements were performed on a Rigaku ZSX Primus-II with a rhodium X-ray source. The repeat thicknesses and *c*-axis lattice parameters were calculated using modified Braggs' law. Out of plane Rietveld refinement and in-plane full pattern Le Bail fits were done in the FullProf suite.[43–45]

Cross-sectional lamellae for STEM imaging were prepared on a FEI Helios 600-dual beam focused ion beam with a side winder ion column using backside milling methods and wedge premilling methods.[46,47] High-angle annular dark field STEM (HAADF-STEM) at Pacific Northwest National Laboratory using a C_s-corrected FEI Titan 80-300 TEM/ STEM at 300 keV.

In-plane resistivity and Hall measurements were performed using the Van der Pauw method.[68] Measurements were preformed under vacuum on a closed cycle He cryostat with magnetic fields ranging from 0 to 1.6 T. Electrical contacts to the sample were made with pressed indium.

Results and Discussion

To explore the existence of a potential new heterostructure containing BiSe, Bi_2Se_3, and $TiSe_2$, precursors with the layer sequences Bi−Se−Bi−Se−Bi−Se−Ti−Se were deposited using the Ti-Se layer thicknesses that were known to form single unit cell thick layers of $TiSe_2$ on annealing. The thickness and composition of the Bi-Se

repeating layers were varied in an attempt to increase the intensity of the reflections of the previously detected heterostructure. Upon heating, numerous precursors crystallized in to a superlattice with a *c*-axis lattice parameter of ~27.5 Å. The diffraction patterns also contained evidence for surface segregated Bi_2Se_3, split reflections suggesting extra layers in the superstructure and/or broad low intensity reflections indicating a lack of structural coherence.[69] The observation of a superlattice with a *c*-axis lattice parameter of ~27.5(1) Å forming over a range of composition, however, suggests that the compound forming must exist in a deep local free energy minimum in the free energy landscape relative to alternative compounds with similar composition.[26,27] The composition range and *c*-axis lattice parameter of ~27.5(1) Å is consistent with a compound that is comprised of one quintuple layer of Bi_2Se_3 (*c* = ~9.5 Å), two bilayers of BiSe ((*c* = ~6 Å), and one layer of $TiSe_2$ (*c* = ~6 Å). Using the stoichiometry of previously reported $BiSe_{1.15}TiSe_2$ and the *a*-lattice parameter of Bi_2Se_3, the expected composition of a $(BiSe)_2$-(Bi_2Se_3)-$(TiSe_2)$ is: 33.57% Bi, 57.60% Se and 8.83% Ti.[70,71] Table 3.1 summarizes the as-deposited compositions determined from X-ray fluorescence measurements, repeat layer thicknesses, and *c*-axis lattice parameter of the superlattice formed after annealing various precursors at 350 °C for 30 minutes.

Table 3.1: Composition, as-deposited repeat thickness, and annealed c-lattice parameter of precursors and characteristics of the diffraction scans.

Sample	%Bi	%Se	%Ti	Repeat thickness As-deposited (Å)	*c*-axis lattice parameter 350 °C (Å)	Comment
1	32.09	58.24	9.67	26.8(1)	27.60(3)	Impurity
2	29.75	60.13	10.12	27.2(2)	27.54(9)	Impurity
3	29.97	60.06	9.98	29.1(2)	27.54(3)	Impurity
4	28.28	62.32	9.39	27.5(4)	27.4(2)	Broad/weak reflections
5	28.28	62.32	9.39	29.2(4)	27.60(9)	Impurity
6	29.71	60.76	9.53	31.8(4)	27.5(2)	Split reflections
7	28.38	62.73	8.89	32.0(5)	27.5(2)	Split reflections

We prepared and investigated the self-assembly of a precursor designed to target $(BiSe)_2$-(Bi_2Se_3)-$(TiSe_2)$ with a slight excess of Se to account for evaporation during annealing. Specular and in-plane X-ray diffraction scans (Figure 1) were collected after annealing for 30 minutes at different temperatures (50 °C increments up to 450 ^{O}C). Surprisingly, there are resolvable Bragg reflections out to ~65° 2θ in the as-deposited sample indicating that diffusion occurs on deposition and a coherent pattern of crystalline layers have already begun to self-assemble. The line width of these broader reflections at higher angles (>10° 2θ) arise from slightly different spacings between the different crystalline layers. These reflections yield a *c*-axis lattice parameter of 27.67(4) Å. The sharp low-angle (<10° 2θ) reflections result from the compositional modulation of the precursor and yield a repeating thickness of the elemental modulation of 27.7(2) Å. As the annealing temperature is increased, the intensity of the higher angle reflections increases and the linewidths decrease indicating that the constituents are becoming more crystalline. The low angle reflections gradually shift to lower angles in

the low temperature regime, moving closer to the angles expected from the higher angle reflections. After annealing at 350 °C, all reflections can be indexed to a single family of reflections, which have the highest intensities and narrowest line widths without evidence of additional phases. We chose this as the optimal annealing temperature, which is the same as that reported for the synthesis of $(BiSe)_{1+\delta}[TiSe_2]_n$. The *c*-axis lattice parameter after the 350°C annealing is 27.54(2) Å), which is slightly larger than the sum of the *c*-axis lattice parameters of the lattice parameters of Bi_2Se_3, $(BiSe)_{1.15}TiSe_2$ and the estimated thickness of an additional BiSe layer (27.05 Å). After annealing the sample at 400°C, additional reflections appear that are consistent with textured Bi_2Se_3 phase segregating from the superlattice. This is likely driven by oxidation of $TiSe_2$, which has previously been observed in metastable $[(BiSe)_{1+\delta}]_m[TiSe_2]_m$ compounds annealed at these temperatures.[63]

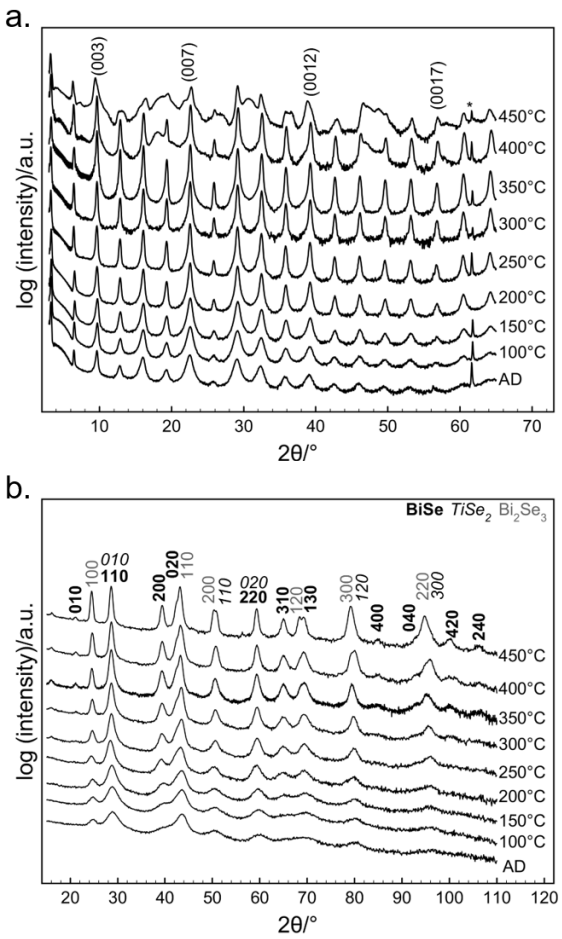

Figure 3.1: Specular diffraction (a.) and in-plane diffraction (b.) patterns of precursor annealed at the indicated temperatures for 30 minutes.

In-plane diffraction of the as-deposited precursor and after annealing at different temperatures is shown in Figure 1b. The as-deposited precursor has Bragg reflections that indicate that nucleation and growth of constituent layers occurs during deposition. The presence of the reflection at ~25° 2θ indicates that small grains of Bi_2Se_3 are present and the reflection at ~40° 2θ indicates the BiSe is also present. The reflections for $TiSe_2$ all overlap with those expected from Bi_2Se_3 and BiSe, so it is not clear that it also nucleates on deposition. As the annealing temperature is increased, the BiSe reflection at ~40° 2θ becomes more defined and distinct from the reflection at ~43° 2θ and the reflection at ~68° 2θ splits into two BiSe reflections. This indicates that the

BiSe layer(s) have a rectangular basal plane as has been reported previously.[70] After the 200 °C anneal, all reflections can be indexed to either BiSe, Bi_2Se_3, or $TiSe_2$ indicating that little or no additional phases are present. After the 250° C anneal, a small reflection at ~16° 2θ is resolved that cannot be indexed to BiSe, Bi_2Se_3 or $TiSe_2$. This suggests that an additional phase may be present or that one of the constituents has undergone a structural distortion forming a supercell. After the 300 ° C anneal, there is an additional small reflection ~21° 2θ that can be indexed as the BiSe (010) reflection. This suggests that BiSe is not forming as a typical face centered rock salt structure as this reflection would be forbidden. The intensity of the two-small low-angle reflections increases during the 350° C and 400° C annealing. After the 450 °C anneal, the relative intensity of the Bi_2Se_3 reflections increases and the $TiSe_2$ reflection intensity decreases. This is most clearly seen by the shift to lower 2θ of the peak at ~96°, which is consistent with a shift in intensity from the $TiSe_2$ (300) reflection to the Bi_2Se_3 (220) reflection. This is consistent with specular diffraction data showing the presence of surface segregated Bi_2Se_3 and suggests that $TiSe_2$ is being oxidized and the released Se reacts with BiSe to form Bi_2Se_3. The in-plane lattice parameters from a full pattern Le Bail fit and *c*-lattice parameter are summarized in Table 3.2. The lattice parameters of $(BiSe)_{1.15}TiSe_2$ are provided for reference.

Table 3.2: Lattice Parameters of $(BiSe)_{1+\delta}(Bi_2Se_3)_{1+\gamma}(BiSe)_{1+\delta}(TiSe_2)$

	$(BiSe)_{1+\delta}(Bi_2Se_3)_{1+\gamma}(BiSe)_{1+\delta}TiSe_2$	$(BiSe)_{1.15}TiSe_2$[70]
BiSe *a* (Å)	4.5706(8)	0.4562(2)
BiSe *b* (Å)	4.2452(6)	0.4242(1)
Bi_2Se_3 a (Å)	4.1754(5)	-
$TiSe_2$ *a* (Å)	3.5932(8)	0.358(6)
$1+\delta$	1.15	1.15
$1+\gamma$	0.74	
c-lattice parameter (Å)	27.54(2)	

To probe to local structure, HAADF-STEM was collected (Figure 2). Figure 2a shows a HAADF-STEM image in which the top and bottom of the film are visible. The image confirms that the sample formed a periodic layered structure throughout. The repeating unit contains one $TiSe_2$ trilayer, one Bi_2Se_3 quintuple-layer, and two BiSe bilayers, consistent with the diffraction data. Interestingly, the BiSe layers formed between the $TiSe_2$ and Bi_2Se_3 layers giving a stacking order of BiSe-Bi_2Se_3-BiSe-$TiSe_2$. This ordering may be due to an inherent instability in placing two or more BiSe bilayers next to one another or may stabilize the structure by reducing the lattice mismatch between the dichalcogenide and Bi_2Se_3, as was hypothesized for $Bi_2Se_3/NbSe_2$ heterostructures.[72] No extended defects are present however a few quintuple layers of surface segregated Bi_2Se_3 are visible suggesting that excess Bi and Se were present in the precursor.

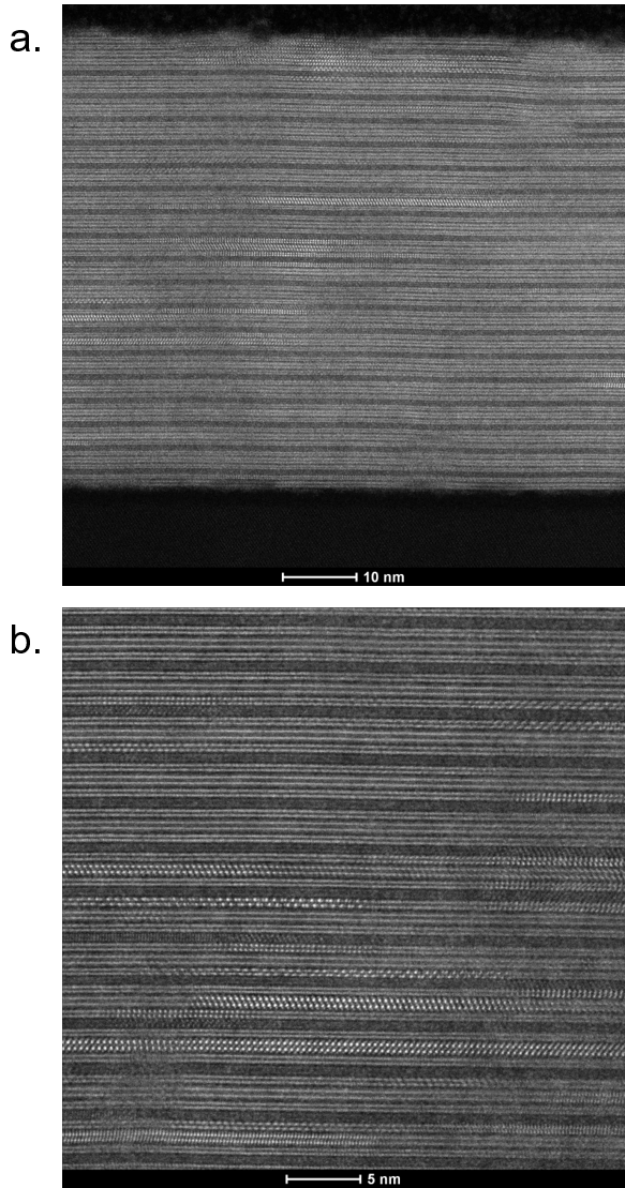

Figure 3.2: Medium magnification HAADF-STEM image (a) and high magnification HAADF-STEM image of precursor annealed at 350 °C for 30 minutes

Figure 2b shows a higher magnification HAADF-STEM image that provides a clearer picture of the local structure. The visible zone axis changes layer-to-layer, confirming turbostratic disorder. All interfaces are atomically abrupt and $TiSe_2$ is present in the expected 1T polytype. Anti-phase boundaries that result in Bi-Bi bonding were previously seen misfit layered compounds $(BiSe)_{1.10}NbSe_2$ and $(BiSe)_{1.09}TaSe_2$[73,74]

and in rotationally disordered ferecrystalline compounds.[75–78] When grains are orientated along a (110) zone axis, anti-phase boundaries are visible and appear regularly spaced.

An initial model for Rietveld refinement of the specular diffraction was prepared by integrating the HAADF-STEM image intensity across approximately five unit-cells. The intensity profile was fit to a sum of Gaussians with the position of each Gaussian corresponding to the position of an atomic plane. The fractional coordinates of each plane were determined by dividing the pixel number corresponding to the atomic plane by the number of pixels within that unit cell. The region of integration (a), intensity profile (b), and a single fitted unit cell (c) are shown in Figure 3.3. The green Gaussians correspond to Bi atoms, the yellow to Se atoms, and the black to Ti. The atomic planes in the BiSe layer were fit as single peaks (blue) despite there being both Bi and Se atoms in each plane because it was not possible to spatially resolve the two atomic species.

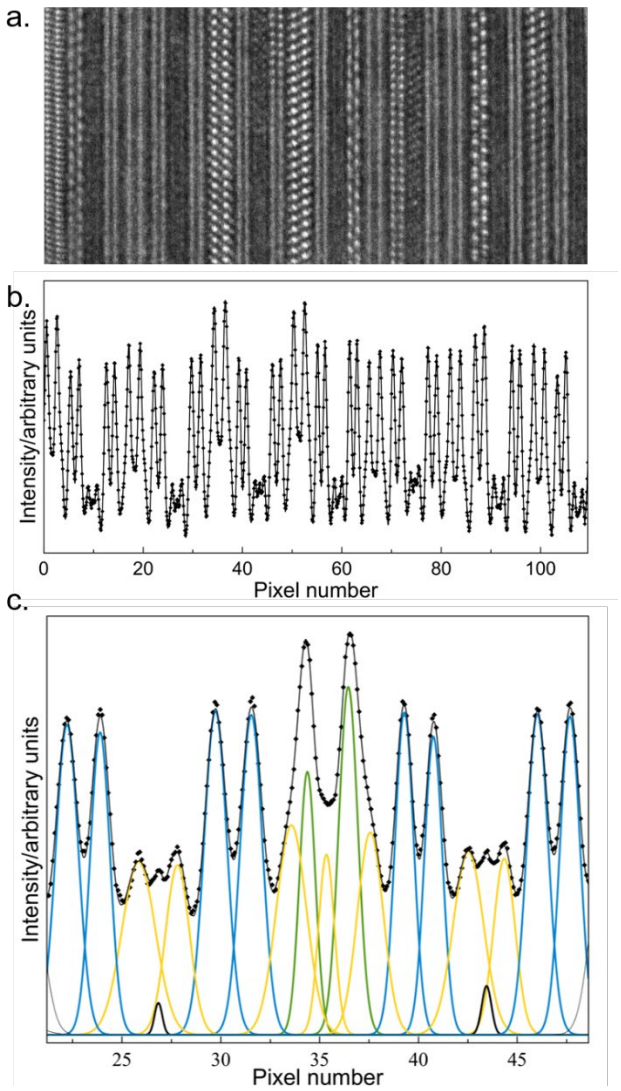

Figure 3.3: High resolution image showing clear atomic columns (a), integrated intensity (b), and integrated intensity of one unit cell with fitted positions of individual gaussian peaks for each atomic plane (c). The black peaks correspond to Ti planes, green to Bi, orange to Se, and blue to BiSe.

The Rietveld refinement of the specular diffraction (left) and the refined structural model (right) are shown in Figure 3.4. The refined *c*-lattice parameter, 27.5598(6) Å, is consistent with that obtain from using modified Bragg's law. Puckering of the BiSe layer, where the cation moves outward towards the dichalcogenide and the anion movers inward, was previously observed in

$(BiSe)_{1+\delta}TiSe_2]_n$ but is not resolvable here. The separation of the Ti and Se atomic planes in $TiSe_2$ is approximately 0.03 Å smaller than the bulk distance.[79] The Bi-Se atomic plane distance in BiSe is comparable to the distance in $(BiSe)_{1+\delta}TiSe_2]_n$ and the $TiSe_2$-BiSe van der Waals gap is approximately comparable to $(BiSe)_{1+\delta}TiSe_2]_3$.[51]

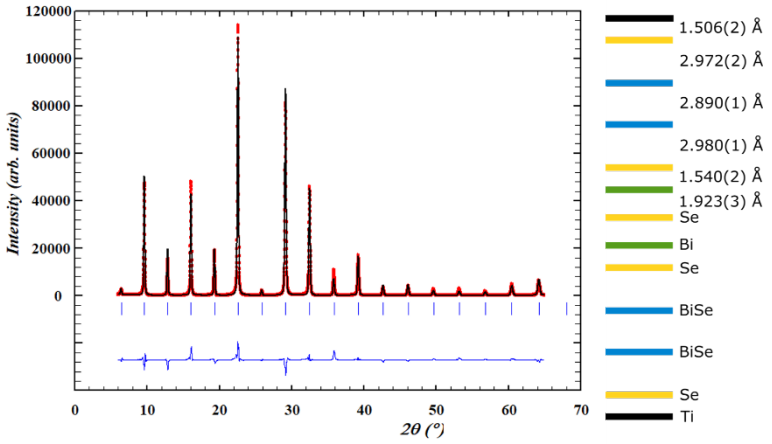

Figure 3.4: Rietveld refinement of specular diffraction pattern (left) and refined model (right)

Analysis of the in-plane diffraction data can also benefit from being refined using the Rietveld approach. A Rietveld refinement of Bi_2Se_3 and $TiSe_2$ was possible using the bulk crystal structures as initial models. Since no bulk structure exists for rock salt BiSe a model must be created. The presences of mixed even and odd reflections indicates that BiSe does not form in the typical face-center rock salt structure and the presence of reflections at lower diffraction angles suggests that a supercell may have formed. To aid creating an initial structural model, the intensity of a STEM image was integrated across the top and bottom Bi-Se atomic plane when viewed down what would be the rock-salt (110) zone axis (Figure 3.5). The greater intensity peaks correspond to Bi atoms and the remaining peaks correspond to Se atoms. Similar to

before, the intensity profile was fit to a sum of Gaussians and the fractional coordinates determined from the ratios of pixels.

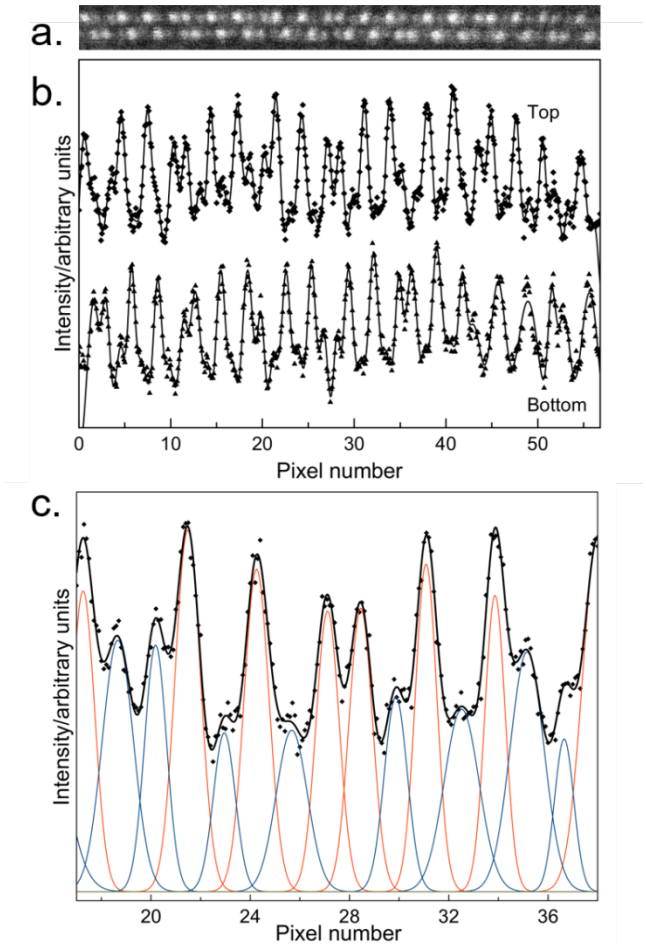

Figure 3.5: High resolution image of BiSe bilayer (a), integrated intensity (b) of the top atomic plane and the bottom atomic plane and integrated intensity of the top plane of one supercell with fitted positions of individual gaussian peaks (c). The red peaks correspond to Bi atoms and blue to Se.

Figure 3.6 depicts the BiSe structure, determined from fitting the STEM image intensities, as seen down what would be the rock salt (110) zone axis. Most notable is the presence of periodic anti-phase boundaries. The anti-phase boundaries are spaced by five Bi-Se bonds and alternate Bi-Bi bond on the top plane and Bi-Bi bond on the bottom plane. These periodic anti-phase boundaries form a supercell that is similar to

that reposted for $BiSe_{1.09}TaSe_2$ misfit layer compound.[74] There is a noticeable distortion that displaces some atoms in the top plane so that they are not directly atop to the atoms in the bottom plane. For example, the Bi atom (red), second from the left is displaced significantly to the left while the pair of Bi and Se atoms (blue) fourth from the left appear to nearly atop each other. These random displacements may cause enough deviation from the rock salt structure to explain the presence of forbidden reflections in the in-plane diffraction pattern. Despite having this initial structural model, it was not possible to refine a model that produced satisfactory intensity for all BiSe reflections, suggesting that additional structural features are present that are not accounted for. A full pattern Le Bail fit was used to refine the lattice parameters of the expanded unit cell determined from the STEM images. The in-plane lattice parameters and refined *c*-axis lattice parameter are summarized in Table 3.3.

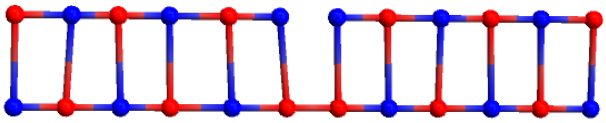

Figure 3.6: Cartoon of BiSe structure determined from the intensity profile of the STEM images. Red corresponds to Bi atoms and blue to Se atoms.

Table 3.3: Lattice Parameters of $(BiSe)_{1+\delta}(Bi_2Se_3)_{1+\gamma}(BiSe)_{1+\delta}(TiSe_2)$

BiSe *a* (Å)	27.2400
BiSe *b* (Å)	4.2774
Bi_2Se_3 a (Å)	4.1772
$TiSe_2$ *a* (Å)	5.9376
c-lattice parameter (Å)	27.5598(6)

To gain insight into the electronic properties of the new heterostructure, temperature dependent resistivity and hall effect measurements were performed between 20 and 295 K. Figure 3.7 shows the temperature dependent resistivity of the

new heterostructure compared to $(BiSe)_{1.15}TiSe_2$. There is similar metallic temperature dependence between the two materials. Surprisingly, the addition of the low conductivity Bi_2Se_3 layer and additional BiSe layer reduces the resistivity. If this compound were approximated as a simple composite one would expect an increase in resistivity since the addition of Bi_2Se_3 and BiSe increases the volume fraction of semiconducting material. This deviation from simple composite behavior suggests complex interlayer interactions. To gain a better understanding of what might be causing the unexpected behavior the resistivity data was fit using the Bloch-Gruneisen model,

$$\rho(T) = \rho_0 + \Re\left(\frac{T}{\theta_D}\right)^5 \int_0^{\theta_D} \frac{z^5}{(e^z - 1)(1 - e^{-z})} dz$$

Where ρ_0 is the residual resistivity, $\Re$ is the electron-phonon interaction constant and θ_D is the Debye temperature. The fitted parameters are reported in Table 3.4. The new heterostructure has a substantially lower Debye temperature than $(BiSe)_{1.15}TiSe_2$. Assuming that $TiSe_2$ dominates the in-plane conduction then the size of first Brillouin zone remains relatively unchanged between $(BiSe)_{1.15}TiSe_2$ and $(BiSe)_{1+\delta}(Bi_2Se_3)_{1+\gamma}(BiSe)_{1+\delta}TiSe_2$ since the size of the Brillouin zone is determined by the dimension and volume of the real space lattice and $TiSe_2$ has approximately the same lattice constant in both materials. Thus, the decrease in the Debye temperature implies a change in the distribution of phonons in the material since $\theta_D = \omega_D \hbar / k_B$ and $\omega_D = q_D / s$ where ω_D is the Debye frequency, q_D is the radius of the Debye sphere whose volume is equal to the volume of the first Brillouin zone in *k*-space, and *s* is the sound velocity in the material. Since we assumed that q_D is approximately the same for

$TiSe_2$ in both materials, the change in the Debye temperature must be caused by a change in the sound velocity in the lattice, which is equal to the propagation velocity of the acoustic phonons. The lower electron-phonon interaction constant of the $(BiSe)_{1+\delta}(Bi_2Se_3)_{1+\gamma}(BiSe)_{1+\delta}TiSe_2$ further implies that the change in conductivity is due to a change in the distribution on phonon modes. The change in the phonon modes is not unexpected given that different interfaces are present in $(BiSe)_{1+\delta}(Bi_2Se_3)_{1+\gamma}(BiSe)_{1+\delta}TiSe_2$ as well as a different density of anti-phase boundaries in the BiSe layers. While the presences of additional interfaces and structural distortions is a plausible explanation for the reduced Debye temperature and electron phonon-interaction constant, potential conduction through topologically protected metallic state of the Bi_2Se_3 layers cannot be ruled out.

Table 3.4: Bloch-Gruneisen Fit Parameters.

	$(BiSe)_{1+\delta}(Bi_2Se_3)_{1+\gamma}(BiSe)_{1+\delta}TiSe_2$	$(BiSe)_{1.15}TiSe_2$
ρ_0	3.016(5)	4.54(1)
$\Re$	6.4(1)	12.4(5)
θ_D	262(6)	490(16)

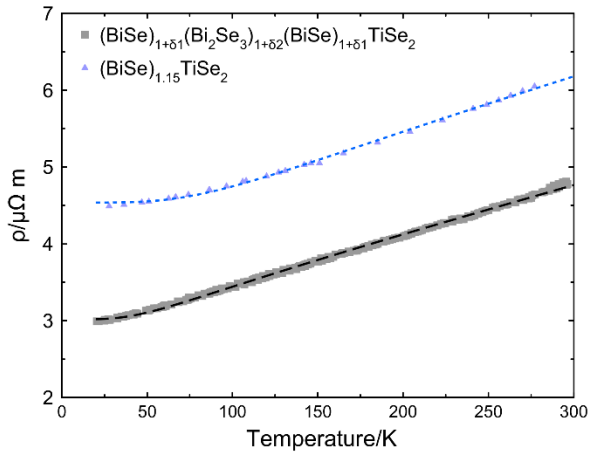

Figure 3.7: Temperature dependent resistivity of $(BiSe)_{1+\delta}(Bi_2Se_3)_{1+\gamma}(BiSe)_{1+\delta}TiSe_2$ compared to $(BiSe)_{1.15}TiSe_2$

Temperature dependent Hall effect measurements were conducted (3.8a) from which the carrier concentration (3.8c) and carrier mobility (3.8c) were determined. The Hall coefficient is negative across the temperature range indicating that electrons are the majority carrier type. The Hall coefficient decrease slightly which is consistent with a low conductivity metal. The carrier concentration shown negligible temperature dependence, also consistent with a metal. The carrier concentration is lower than $(BiSe)_{1.15}TiSe_2$ even with the additional charge donating BiSe layer per $TiSe_2$. We hypothesize that the number of anti-phase boundaries in $(BiSe)_{1+\delta}(Bi_2Se_3)_{1+\gamma}(BiSe)_{1+\delta}TiSe_2$ is greater than in $(BiSe)_{1.15}TiSe_2$. Since Bi-Bi bounds localize electrons, the greater concentration of anti-phase boundaries decreases the number of electrons per BiSe layer that are available to donate to the $TiSe_2$ conduction band.

The mobility, calculated assuming a single parabolic band, is greater than the mobility of $(BiSe)_{1.15}TiSe_2$ and shows some temperature dependence. The increased mobility suggests that there is less scattering from phonons, consistent with the

decreased electron-phonon interaction constant. The increases mobility may also be related to the decreases puckering of the BiSe layers. These transport data show that the new heterostructure cannot be modeled as a simple composite of the constituents and indicated that the layers interact with one another to produce emergent behavior.

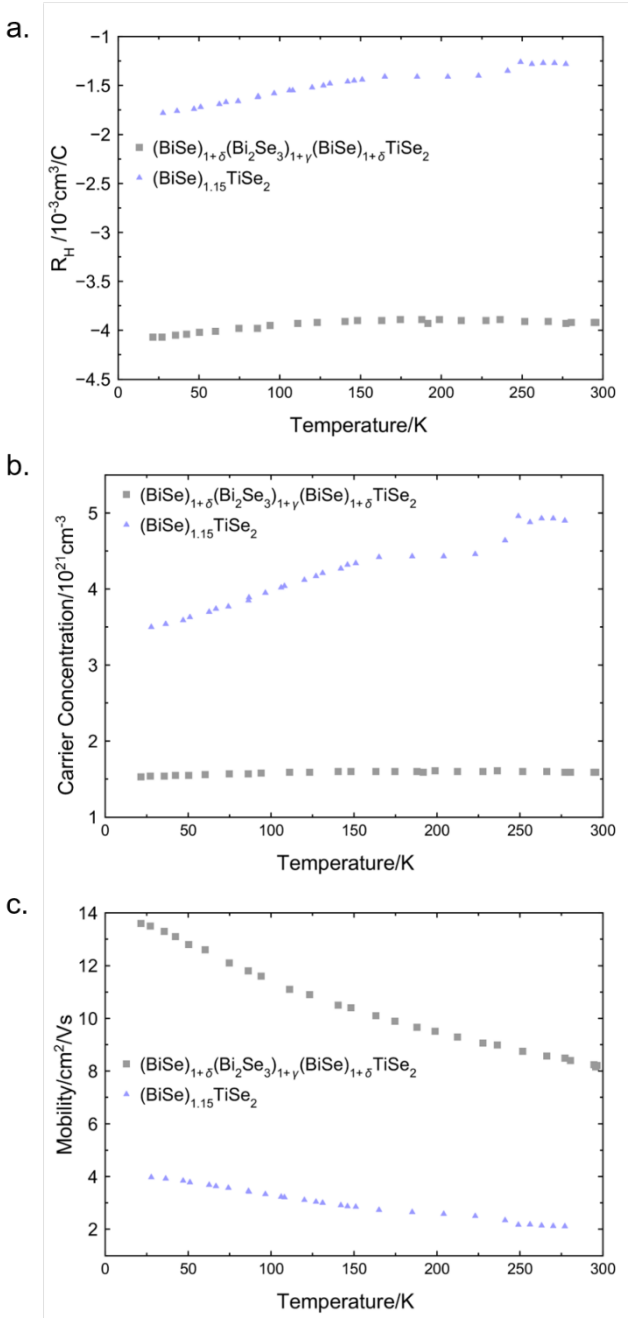

Figure 3.8: Temperature dependent Hall coefficient(a) , carrier concentration (b), and carrier mobility of $(BiSe)_{1+\delta}(Bi_2Se_3)_{1+\gamma}(BiSe)_{1+\delta}TiSe_2$ compared to $(BiSe)_{1.15}TiSe_2$.

Conclusion

The synthesis, structure and properties of a new three constituent heterostructure containing BiSe, Bi_2Se_3, and $TiSe_2$ is reported. The compound formed over a wide precursor composition range and began to self-assemble on deposition indicating that it exists in a relatively deep free energy minimum. The structure of the Bi_2Se_3 and $TiSe_2$ layers were similar to those seen in other heterostructures and bulk. High-resolution electron microscopy images revealed that the BiSe layer contained periodic anti-phase boundaries that distort the structure from a typical rock salt structure. Electron transport measurements show an unexpected decrease in resistivity and carrier concentration that may be due to a change in the distribution of phonons and increased density of anti-phase boundaries. These results demonstrate that heterostructures cannot always be treated as simple composites because interlayer interactions lead to emergent behavior. We have shown that new materials can be formed with designed nanoarchitecture by incorporating compounds known to form infinitely adaptable series, such as Bi_2Se_3, into heterostructures. Given the adaptability of the Bi_xSe_y family of compounds, one could potentially prepare many series of Bi_xSe_y-TSe_2 compounds by varying the composition parameter x and y and the transition metal T.

Conclusions, Summary, and Outlook for Future Work

The formation and decomposition of a series of kinetically formed compounds and the structure and properties of a new compound are reported and discussed. All compounds formed through self-assembly of designed precursors that were prepared by physical vapor deposition.

Kinetically stable BiSe-$TiSe_2$ containing heterostructures, $[(BiSe)_{1+\delta}]_m[TiSe_2]_m$ for $m \leq 3$ were synthesized and studied using a combination of X-ray diffraction, high-resolution electron microscopy, and differential scanning calorimetry. All compounds began self-assembling on deposition and showed evidence of the desired phases. At elevated annealing temperatures both the $m = 2$ and the $m = 3$ compounds structurally rearranged into the $m = 1$ compound as indicated by the specular diffraction pattern and electron microscopy images of the $m = 2$. These results demonstrated that chemists can qualitatively determine the topology of a free energy landscape by studying homologous series of compounds. Before decomposing, additional reflections were observed in the specular diffraction pattern of the $m = 3$ that indicated the presence of a heterostructure with a smaller *c*-axis lattice parameter. Bi_2Se_3 was also present in the samples at all annealing temperatures. This prompted an investigation into the possibility of a new heterostructure containing BiSe, Bi_2Se_3, and $TiSe_2$.

A new three constituent heterostructure, $(BiSe)_{1+\delta}(Bi_2Se_3)_{1+\gamma}(BiSe)_{1+\delta}TiSe_2$, was synthesized and its structure and properties were studied. The compound formed with Bi_2Se_3 and $TiSe_2$ adopting structure similar to their bulk structures. The in-plane diffraction patterns indicated the BiSe did not adopt a typical rock salt like structure and may have formed a supercell. High resolution microscopy images showed that the BiSe

layers contained periodic anti-phase boundaries. Electron transport measurements revealed surprising behavior with lower resistivity and higher carrier mobility than $(BiSe)_{1.15}TiSe_2$. These results demonstrate that heterostructures cannot be model as simple composites since interlayer interactions can lead to emergent behavior. Since Bi_2Se_3 is one member of the Bi_xSe_y infinitely adaptable series, a series were new compounds can be created by expanding the dimension of either the stacks of Bi_2Se_3 quintuple-layers or the Bi bilayers, it may be possible to prepare a new series of $(BiSe)_{1+\delta}[(Bi_2Se_3)_{1+\gamma}]_m(BiSe)_{1+\delta}TiSe_2$ compounds by increasing *m*. Initial work indicates that this hypothesis is correct and compounds with $m = 2$ and 3 have been prepared. These initial results suggest that numerous new compounds could be formed with the layering sequence $(BiSe)_{1+\delta}[(Bi_2Se_3)_{1+\gamma}]_m(BiSe)_{1+\delta}[TSe2]_n$ by varying the transition metal species, T, and by varying *m* and *n*.

Bibliography

(1) Disalvo, F. J. Challenges and Opportunities in Solid-State Chemistry. *Pure Appl. Chem* **2000**, *72* (10), 1799–1807.

(2) Stein, A.; Keller, S. W.; Mallouk, T. E. Turning down the Heat: Design and Mechanism in Solid-State Synthesis. *Science* **1993**, *259* (5101), 1558–1564.

(3) Kanatzidis, M. G.; Pöttgen, R.; Jeitschko, W. The Metal Flux: A Preparative Tool for the Exploration of Intermetallic Compounds. *Angew. Chemie - Int. Ed.* **2005**, *44* (43), 6996–7023.

(4) Kanatzidis, M. G. Structural Evolution and Phase Homologies For "design" and Prediction of Solid-State Compounds. *Acc. Chem. Res.* **2005**, *38* (4), 359–368.

(5) Johnson, D. C. Controlled Synthesis of New Compounds Using Modulated Elemental Reactants. *Curr. Opin. Solid State Mater. Sci.* **1998**, *3* (2), 159–167.

(6) Fischer, D.; Jansen, M. Low-Activation Solid-State Syntheses by Reducing Transport Lengths to Atomic Scales as Demonstrated by Case Studies on $AgNO_3$ and AgO. *J. Am. Chem. Soc.* **2002**, *124* (14), 3488–3489.

(7) Hamann, D. M.; Hadland, E.; Johnson, D. C. Heterostructures Containing Dichalcogenides- New Materials with Predictable Nanoarchitectures and Novel Emergent Properties. *Semicond. Sci. Technol.* **2017**, *32* (9), 93004.

(8) Harris, F. R.; Standridge, S.; Feik, C.; Johnson, D. C. Design and Synthesis of $[(Bi_2Te_3)_x(TiTe_2)_y]$ Superlattices. *Angew. Chem. Int. Ed. Engl.* **2003**, *42* (43), 5296–5299.

(9) Chhowalla, M.; Shin, H. S.; Eda, G.; Li, L.-J.; Loh, K. P.; Zhang, H. The Chemistry of Two-Dimensional Layered Transition Metal Dichalcogenide Nanosheets. *Nat. Chem.* **2013**, *5* (4), 263–275.

(10) Frindt, R. F. Superconductivity in Ultrathin $NbSe_2$ Layers. *Phys. Rev. Lett.* **1972**, *28* (5), 299–301.

(11) Morosan, E.; Zandbergen, H. W.; Dennis, B. S.; Bos, J. W. G.; Onose, Y.; Klimczuk, T.; Ramirez, A. P.; Ong, N. P.; Cava, R. J. Superconductivity in Cu_xTiSe_2. *Nat. Phys.* **2006**, *2* (8), 544–550.

(12) Wilson, J. A.; Di Salvo, F. J.; Mahajan, S. Charge-Density Waves in Metallic, Layered, Transition-Metal Dichalcogenides. *Phys. Rev. Lett.* **1974**, *32* (16), 882–885.

(13) Deng, K.; Wan, G.; Deng, P.; Zhang, K.; Ding, S.; Wang, E.; Yan, M.; Huang, H.; Zhang, H.; Xu, Z.; et al. Experimental Observation of Topological Fermi Arcs in Type-II Weyl Semimetal $MoTe_2$. *Nat. Phys.* **2016**, *12* (December), 1105–1110.

(14) Desai, S. B.; Madhvapathy, S. R.; Sachid, A. B.; Llinas, J. P.; Wang, Q.; Ahn, G. H.; Pitner, G.; Kim, M. J.; Bokor, J.; Hu, C.; et al. MoS_2 Transistors with 1-Nanometer Gate Lengths. *Science (80-.).* **2016**, *354* (6308), 99–102.

(15) Beekman, M.; Heideman, C. L.; Johnson, D. C. Ferecrystals: Non-Epitaxial Layered Intergrowths. *Semicond. Sci. Technol. Semicond. Sci. Technol. Semicond. Sci. Technol* **2014**, *29* (29), 64012–64012.

(16) Lin, Q.; Smeller, M.; Heideman, C. L.; Zschack, P.; Koyano, M.; Anderson, M. D.; Kykyneshi, R.; Keszler, D. A.; Anderson, I. M.; Johnson, D. C. Rational Synthesis and Characterization of a New Family of Low Thermal Conductivity Misfit Layer Compounds $[(PbSe)_{0.99}]_m(WSe_2)_n$. *Chem. Mater.* **2010**, *22* (3), 1002–1009.
(17) Chiritescu, C.; Mortensen, C.; Cahill, D. G.; Johnson, D.; Zschack, P. Lower Limit to the Lattice Thermal Conductivity of Nanostructured Bi_2Te_3-Based Materials. *J. Appl. Phys.* **2009**, *106* (7), 73503.
(18) Esters, M.; Alemayehu, M. B.; Jones, Z.; Nguyen, N. T.; Anderson, M. D.; Grosse, C.; Fischer, S. F.; Johnson, D. C. Synthesis of Inorganic Structural Isomers by Diffusion-Constrained Self-Assembly of Designed Precursors: A Novel Type of Isomerism. *Angew. Chemie - Int. Ed.* **2015**, *54* (4), 1130–1134.
(19) Alemayehu, M. B.; Falmbigl, M.; Ta, K.; Grosse, C.; Westover, R. D.; Bauers, S. R.; Fischer, S. F.; Johnson, D. C. Structural and Electrical Properties of $([SnSe]_{1+\delta})_m(NbSe_2)_1$ Compounds: Single $NbSe_2$ Layers Separated by Increasing Thickness of SnSe. *Chem. Mater.* **2015**, *27* (3), 867–875.
(20) Wang, X. L.; Sakurai, H.; Takayarria-Muromachi, E. Synthesis, Structures, and Magnetic Properties of Novel Roddlesden-Popper Homologous Series $Sr_{n+1}Co_nO3_{n+1}$ (N = 1,2,3,4, and Infinity). *J. Appl. Phys.* **2005**, *97* (10), 10M519.
(21) Tian, W.; Haeni, J. H.; Schlom, D. G.; Hutchinson, E.; Sheu, B. L.; Rosario, M. M.; Schiffer, P.; Liu, Y.; Zurbuchen, M. A.; Pan, X. Q. Epitaxial Growth and Magnetic Properties of the First Five Members of the Layered $Sr_{n+1}Ru_nO_{3n+1}$ Oxide Series. *Appl. Phys. Lett.* **2007**, *90* (2), 22507.
(22) Maeno, Y.; Hashimoto, H.; Yoshida, K.; Nishizaki, S.; Fujita, T.; Bednorz, J. G.; Lichtenberg, F. Superconductivity in a Layered Perovskite without Copper. *Nature* **1994**, *372* (6506), 532–534.
(23) Moritomo, Y.; Asamitsu, A.; Kuwahara, H.; Tokura, Y. Giant Magnetoresistance of Manganese Oxides with a Layered Perovskite Structure. *Nature* **1996**, *380* (6570), 141–144.
(24) Kabbour, H.; Cario, L. $Ae_2Sb_2X_4F_2$ (Ae = Sr, Ba): New Members of the Homologous Series $Ae_2M_{1+n}X_{3+n}F_2$ Designed from Rock Salt and Fluorite 2D Building Blocks. *Inorg. Chem.* **2006**, *45* (6), 2713–2717.
(25) Cario, L.; Kabbour, H.; Meerschaut, A. Designing New Inorganic Compounds from 2D Building Blocks. *Chem. Mater.* **2005**, *17* (2), 234–236.
(26) Schön, J. C.; Jansen, M. First Step Towards Planning of Syntheses in Solid-State Chemistry: Determination of Promising Structure Candidates by Global Optimization. *Angew. Chemie Int. Ed. English* **1996**, *35* (12), 1286–1304.
(27) Jansen, M.; Schön, J. C. "Design" in Chemical Synthesis—An Illusion? *Angew. Chemie Int. Ed.* **2006**, *45* (21), 3406–3412.
(28) Ohno, Y. Electronic Structure of the Misfir-Layer Compounds $PbTiS_3$ and $SnNbS_3$. *Phys. Rev. B* **1991**, *44* (3), 1281–1291.
(29) Ettema, A. R. H. F.; Haas, C. An X-Ray Photoemission Spectroscopy Study of Interlayer Charge Transfer in Some Misfit Layer Compounds. *J. Phys. Condens. Matter* **1993**, *5* (23), 3817–3826.

(30) Ettema, A. R. H. F.; Haas, C.; Turner, T. S. Strong Multiple Resonances in the Photoemission Spectra of Transition-Metal-Layer and Misfit-Layer Compounds. *Phys. Rev. B* **1993**, *47* (19), 12794–12805.
(31) Fang, C. M.; Van Smaalen, S.; Wiegers, G. A.; Haas, C.; de Groot, R. A. Electronic Structure of the Misfit Layer Compound : Band-Structure Calculations and Photoelectron Spectra Electronic Structure of the Misfit Layer Compound $(LaS)_{1.14}NbS_2$: Band-Structure Calculations and Photoelectron Spectra. *J. Phys. Condens. Matter* **1996**, *8* (8), 5367–5382.
(32) Brandt, J.; Kipp, L.; Skibowski, M.; Krasovskii, E. E.; Schattke, W.; Spiecker, E.; Dieker, C.; Jäger, W. Charge Transfer in Misfit Layered Compounds.
(33) Kalläne, M.; Rossnagel, K.; Marczynski-Bühlow, M.; Kipp, L.; Starnberg, H. I.; Stoltz, S. E. Stabilization of the Misfit Layer Compound $(PbS)_{1.13}TaS_2$ by Metal Cross Substitution. *Phys. Rev. Lett.* **2008**, *100* (6).
(34) Beauvais, L. G.; Shores, M. P.; Long, J. R. Cyano-Bridged Re_6Q_8 (Q = S, Se) Cluster-Metal Framework Solids: A New Class of Porous Materials. *Chem. Mater.* **1998**, *10* (12), 3783–3786.
(35) Noh, M.; Thiel, J.; Johnson, D. C. Synthesis of Crystalline Superlattices by Controlled Crystallization of Modulated Reactants. *Science (80-.).* **1995**, *270* (5239), 1181–1184.
(36) Trump, B. A.; Livi, K. J. T.; McQueen, T. M. The New Misfit Compound $(BiSe)_{1.15}(TiSe_2)_2$ and the Role of Dimensionality in the $Cu_x(BiSe)_{1+\delta}(TiSe_2)_n$ Series. *J. Solid State Chem.* **2014**, *209*, 6–12.
(37) Oosawa, Yoshinao; Gotoh, Y.; Akimoto, J. Preparation and Characterization of Bi-Containing Ternary Chalcogenides with Layered Composite Crystal Structure. *J. Alloys Compd.* **1991**, *176*, 319–327.
(38) Gotoh, Y.; Onoda, M.; Uchida, K.; Tanaka, Y.; Iida, T.; Hayakawa, H.; Oosawa, Y. Preparation and Characterization of $BiMX_3$ (M = Ti, V, Nb, Ta; X = S, Se), New Composite-Layered Chalcogenides. *Chem. Lett.* **1989**, *18* (9), 1559–1562.
(39) Merrill, D. R.; Moore, D. B.; Coffey, M. N.; Jansons, A. W.; Falmbigl, M.; Johnson, D. C. Synthesis and Characterization of Turbostratically Disordered $(BiSe)_{1.15}TiSe_2$. *Semicond. Sci. Technol.* **2014**, *29* (6), 64004.
(40) Atkins, R.; Wilson, J.; Zschack, P.; Grosse, C.; Neumann, W.; Johnson, D. C. Synthesis of $[(SnSe)_{1.15}]_m(TaSe_2)_n$ Ferecrystals: Structurally Tunable Metallic Compounds. *Chem. Mater.* **2012**, *24* (23), 4594–4599.
(41) Phung, T. M.; Jensen, J. M.; Johnson, D. C.; Donovan, J. J.; McBurnett, B. G. Determination of the Composition of Ultra-Thin Ni-Si Films on Si: Constrained Modeling of Electron Probe Microanalysis and X-Ray Reflectivity Data. *X-Ray Spectrom.* **2008**, *37* (6), 608–614.
(42) Akselrud, L.; Grin, Y. *WinCSD*: Software Package for Crystallographic Calculations (Version 4). *J. Appl. Crystallogr.* **2014**, *47* (2), 803–805.
(43) Le Bail, A.; Duroy, H.; Fourquet, J. L. Ab-Initio Structure Determination of $LiSbWO_6$ by X-Ray Powder Diffraction. *Mater. Res. Bull.* **1988**, *23* (3), 447–452.
(44) Roisnel, T.; Rodríquez-Carvajal, J. WinPLOTR: A Windows Tool for Powder Diffraction Pattern Analysis. *Mater. Sci. Forum* **2001**, *378–381*, 118–123.
(45) Rodríguez-Carvajal, J. Recent Advances in Magnetic Structure Determination by

Neutron Powder Diffraction. *Phys. B Condens. Matter* **1993**, *192* (93), 55–69.
(46) Kang, H.-J.; Kim, J.; Oh, J.; Back, T.; Kim, H. Ultra-Thin TEM Sample Preparation with Advanced Backside FIB Milling Method. *Microsc. Microanal.* **2010**, *16* (S2), 170–171.
(47) Schaffer, M.; Schaffer, B.; Ramasse, Q. Sample Preparation for Atomic-Resolution STEM at Low Voltages by FIB. *Ultramicroscopy* **2012**, *114*, 62–71.
(48) Fullerton, E. E.; Schuller, I. K.; Vanderstraeten, H.; Bruynseraede, Y. Structural Refinement of Superlattices from X-Ray Diffraction. *Phys. Rev. B* **1992**, *45* (16), 9292–9310.
(49) Anderson, M. D.; Heideman, C. L.; Lin, Q.; Smeller, M.; Kokenyesi, R.; Herzing, A. A.; Anderson, I. M.; Keszler, D. A.; Zschack, P.; Johnson, D. C. Size-Dependent Structural Distortions in One-Dimensional Nanostructures. *Angew. Chemie - Int. Ed.* **2013**, *52* (7), 1982–1985.
(50) Beekman, M.; Disch, S.; Rouvimov, S.; Kasinathan, D.; Koepernik, K.; Rosner, H.; Zschack, P.; Neumann, W. S.; Johnson, D. C. Controlling Size-Induced Phase Transformations Using Chemically Designed Nanolaminates. *Angew. Chemie - Int. Ed.* **2013**, *52* (50), 13211–13214.
(51) Wood, S. R.; Merrill, D. R.; Falmbigl, M.; Moore, D. B.; Ditto, J.; Esters, M.; Johnson, D. C. Tuning Electrical Properties through Control of TiSe2 Thickness in $(BiSe)_{1+\delta}(TiSe_2)_n$ Compounds. *Chem. Mater.* **2015**, *27* (17), 6067–6076.
(52) Hyde, B. G.; Bagshaw, A. N.; Andersson, S.; O'Keeffe, M. Some Defect Structures in Crystalline Solids. *Annu. Rev. Mater. Sci.* **1974**, *4* (1), 43–92.
(53) Mitchson, G.; Falmbigl, M.; Ditto, J.; Johnson, D. C. Antiphase Boundaries in the Turbostratically Disordered Misfit Compound $(BiSe)_{1+\delta}NbSe_2$.
(54) Mitchson, G.; Hadland, E.; Göhler, F.; Wanke, M.; Esters, M.; Ditto, J.; Bigwood, E.; Ta, K.; Hennig, R. G.; Seyller, T.; et al. Structural Changes in 2D BiSe Bilayers as N Increases in $(BiSe)_{1+\delta}(NbSe_2)_n$ (N = 1-4) Heterostructures. *ACS Nano* **2016**, *10* (10), 9489–9499.
(55) Dang, W.; Peng, H.; Li, H.; Wang, P.; Liu, Z. Epitaxial Heterostructures of Ultrathin Topological Insulator Nanoplate and Graphene. *Nano Lett.* **2010**, *10* (8), 2870–2876.
(56) Moore, J. Topological Insulators: The next Generation. *Nat. Publ. Gr.* **2009**, *5*.
(57) Moore, J. E. The Birth of Topological Insulators. *Nature*. 2010, pp 194–198.
(58) Sato, M.; Ando, Y. Topological Superconductors: A Review. *Reports on Progress in Physics*. 2017, p 76501.
(59) Schnyder, A. P. Topological Insulators and Superconductors IV. *Notes* **2015**.
(60) Zhao, Y.; Chang, C.-Z.; Jiang, Y.; DaSilva, A.; Sun, Y.; Wang, H.; Xing, Y.; Wang, Y.; He, K.; Ma, X.; et al. Demonstration of Surface Transport in a Hybrid Bi_2Se_3/Bi_2Te_3 Heterostructure. *Sci. Rep.* **2013**, *3* (1), 3060.
(61) Kim, J.; Park, S.; Jang, H.; Koirala, N.; Lee, J. B.; Kim, U. J.; Lee, H. S.; Roh, Y. G.; Lee, H.; Sim, S.; et al. Highly Sensitive, Gate-Tunable, Room-Temperature Mid-Infrared Photodetection Based on Graphene-Bi_2Se_3 Heterostructure. *ACS Photonics* **2017**, *4* (3), 482–488.

(62) Zhang, Q.; Zhang, Z.; Zhu, Z.; Schwingenschlögl, U.; Cui, Y. Exotic Topological Insulator States and Topological Phase Transitions in Sb_2Se_3-Bi_2Se_3 Heterostructures. *ACS Nano* **2012**, *6* (3), 2345–2352.
(63) Lygo, A. C.; Hamann, D. M.; Moore, D. B.; Merrill, D. R.; Ditto, J.; Esters, M.; Orlowicz, J.; Wood, S. R.; Johnson, D. C. Kinetically Controlled Formation and Decomposition of Metastable $[(BiSe)_{1+\delta}]_m[TiSe_2]_m$ Compounds. *J. Am. Chem. Soc.* **2018**, *140* (9), 3385–3393.
(64) Zhang, H.; Liu, C.-X.; Qi, X.-L.; Dai, X.; Fang, Z.; Zhang, S.-C. Topological Insulators in Bi_2Se_3, Bi_2Te_3 and Sb_2Te_3 with a Single Dirac Cone on the Surface. *Nat. Phys.* **2009**, *5* (6), 438–442.
(65) Zhang, Y.; He, K.; Chang, C. Z.; Song, C. L.; Wang, L. L.; Chen, X.; Jia, J. F.; Fang, Z.; Dai, X.; Shan, W. Y.; et al. Crossover of the Three-Dimensional Topological Insulator $Bi_2Se_3$to the Two-Dimensional Limit. *Nat. Phys.* **2010**, *6* (8), 584–588.
(66) Tobias Forster, Peter Kruger, M. R. Ab Initio Studies of Adatom- and Vacancy-Induced Band Bending in Bi_2Se_3. *Phys. Rev. B* **2015**.
(67) Valla, T.; Ji, H.; Schoop, L. M.; Weber, A. P.; Pan, Z.; Sadowski, J. T.; Vescovo, E.; Fedorov, A. V; Caruso, A. N.; Gibson, Q. D. Topological Semimetal in a Bi-Bi_2Se_3 Infinitely Adaptive Superlattice Phase. **2012**, *241101*, 3–7.
(68) van der Pauw, L. J. A Method of Measuring Specific Resistivity and Hall Effect of Discs of Arbitrary Shape. *Philips Res. Reports* **1958**, *13* (1), 1–11.
(69) Beekman, M.; Rodriguez, G.; Atkins, R.; Kunert, J.; Moore, D. B.; Johnson, D. C. Detection of Nanoscale Embedded Layers Using Laboratory Specular X-Ray Diffraction. *J. Appl. Phys.* **2015**, *117* (18).
(70) Merrill, D. R.; Moore, D. B.; Coffey, M. N.; Jansons, A. W.; Falmbigl, M.; Johnson, D. C. Synthesis and Characterization of Turbostratically Disordered $(BiSe)_{1.15}TiSe_2$. *Semicond. Sci. Technol.* **2014**, *29* (6), 64004–64006.
(71) Lind, H.; Lidin, S. A General Structure Model for Bi-Se Phases Using a Superspace Formalism. *Solid State Sci.* **2003**, *5* (1), 47–57.
(72) Wang, M.-X.; Li, P.; Xu, J.-P.; Liu, Z.-L.; Ge, J.-F.; Wang, G.-Y.; Yang, X.; Xu, Z.-A.; Ji, S.-H.; Gao, C. L.; et al. Interface Structure of a Topological Insulator/ Superconductor Heterostructure. *New J. Phys.* **2014**, *1614* (123043), 1367–263000.
(73) Zhou, W. Y.; Meetsma, A.; de Boer, J. L.; Wiegers, G. A. Characterization and Electrical Transport Properties of the Misfit Layer Compounds $(BiSe)_{1.10}NbSe_2$ and $(BiSe)_{1.09}TaSe_2$. *Mater. Res. Bull.* **1992**, *27* (5), 563–572.
(74) Petříček, V.; Cisarova, I.; De Boer, J. L.; Zhou, W.; Meetsma, A.; Wiegers, G. A.; Van Smaalen, S. The Modulated Structure of the Commensurate Misfit-layer Compound $(BiSe)_{1.09}TaSe_2$. *Acta Crystallogr. Sect. B* **1993**, *49* (2), 258–266.
(75) Wood, S. R.; Merrill, D. R.; Falmbigl, M.; Moore, D. B.; Ditto, J.; Esters, M.; Johnson, D. C. Tuning Electrical Properties through Control of TiSe 2 Thickness in $(BiSe)_{1+\delta}(TiSe_2)_n$ Compounds. *Chem. Mater.* **2015**, *27* (17), 6067–6076.

(76) Wood, S. R.; Merrill, D. R.; Mitchson, G.; Lygo, A. C.; Bauers, S. R.; Hamann, D. M.; Sutherland, D. R.; Ditto, J.; Johnson, D. C. Modulation Doping in Metastable Heterostructures via Kinetically Controlled Substitution. *Chem. Mater.* **2016**, acs.chemmater.6b04688.
(77) Mitchson, G.; Falmbigl, M.; Ditto, J.; Johnson, D. C. Antiphase Boundaries in the Turbostratically Disordered Misfit Compound $(BiSe)_{1+\delta}NbSe_2$. *Inorg. Chem.* **2015**, *54* (21), 10309–10315.
(78) Mitchson, G.; Hadland, E.; Göhler, F.; Wanke, M.; Esters, M.; Ditto, J.; Bigwood, E.; Ta, K.; Hennig, R. G.; Seyller, T.; et al. Structural Changes in 2D BiSe Bilayers as N Increases in $(BiSe)_{1+\delta}(NbSe2)_n$ (N = 1–4) Heterostructures. *ACS Nano* **2016**, *10* (10), 9489–9499.
(79) Riekel, C. Structure Refinement of $TiSe_2$ by Neutron Diffraction. *J. Solid State Chem.* **1976**, *17* (4), 389–392.